Origin and Properties of Hydrothermal Tremor at Lone Star Geyser, Yellowstone National Park, USA

Avinash Nayak[1,2] ID, **Michael Manga[1]** ID, **Shaul Hurwitz[3]** ID, **Atsuko Namiki[4]** ID, and **Phillip B. Dawson[3]** ID

[1]Department of Earth and Planetary Science, University of California, Berkeley, Berkeley, CA, USA, [2]Now at Earth and Environmental Sciences Area, Lawrence Berkeley National Laboratory, Berkeley, CA, USA, [3]U.S. Geological Survey, Moffett Field, CA, USA, [4]School of Integrated Arts and Sciences, Hiroshima University, Hiroshima, Japan

Abstract Geysers are rare geologic features that intermittently discharge liquid water and steam driven by heating and decompression boiling. The cause of variability in eruptive styles and the associated seismic signals are not well understood. Data collected from five broadband seismometers at Lone Star Geyser, Yellowstone National Park are used to determine the properties, location, and temporal patterns of hydrothermal tremor. The tremor is harmonic at some stages of the eruption cycle and is caused by near-periodic repetition of discrete seismic events. Using the polarization of ground motion, we identify the location of tremor sources throughout several eruption cycles. During preplay episodes (smaller eruptions preceding the more vigorous major eruption), tremor occurs at depths of 7–10 m and is laterally offset from the geyser's cone by ~5 m. At the onset of the main eruption, tremor sources migrate laterally and become shallower. As the eruption progresses, tremor sources migrate along the same path but in the opposite direction, ending where preplay tremor originates. The upward and then downward migration of tremor sources during eruptions are consistent with warming of the conduit followed by evacuation of water during the main eruption. We identify systematic relations among the two types of preplays, discharge, and the main eruption. A point-source moment tensor fit to low-frequency waveforms of an individual tremor event using half-space velocity models indicates average $V_S \gtrsim 0.8$ km/s, source depths ~4–20 m, and moment tensors with primarily positive isotropic and compensated linear vector dipole moments.

1. Introduction

Geysers episodically erupt liquid water, steam, and noncondensable gas at near-boiling temperatures. Geyser-like behavior can be diverse in terms of eruption duration, eruption intervals, height of the eruption column, sensitivity to environmental factors, and the pattern of smaller eruptions called preplays that sometimes precede the more vigorous major eruptions. The eruptions are understood to be driven by the conversion of thermal to kinetic energy during decompression of ascending water. Presence of water and heat sources, and fractures and cavities to trap rising fluids are all thought to contribute to geyser diversity (Hurwitz & Manga, 2017).

Seismic signals are particularly informative about subsurface processes during the eruption cycle. Early studies that recorded seismic signals at Old Faithful Geyser (OFG) in the Upper Geyser Basin (UGB) in Yellowstone National Park (YNP) (Figure 1) detected tremor activity that varied throughout the eruption cycle (Nicholls & Rinehart, 1967; Rinehart, 1965). Later, Kieffer (1984) suggested that the relatively isolated source of seismic noise at OFG exhibits behavior similar to that observed at many volcanoes, including harmonic tremor before and during eruptions and periods of seismic quiescence prior to eruptions. Kedar et al. (1996) linked discrete-to-continuous seismic signals recorded by seismometers deployed around OFG to pressure transients recorded by pressure sensors in the geyser's conduit. They inferred that the pressure signals in the water column were caused by continuous collapse of rising steam bubbles leading to the heating of the water (Kedar et al., 1998). Processing the data described in Kedar et al. (1998) and using a beamforming-like method (Cros et al., 2011), Vandemeulebrouck et al. (2013) mapped the temporal evolution of hydrothermal tremor source locations during a few eruption cycles at OFG. The locations reveal a fissure-like conduit through which tremor sources rise leading up to an eruption. They also identified a reservoir laterally offset by ~15 m from the surface location of the geyser cone, which is seismically active
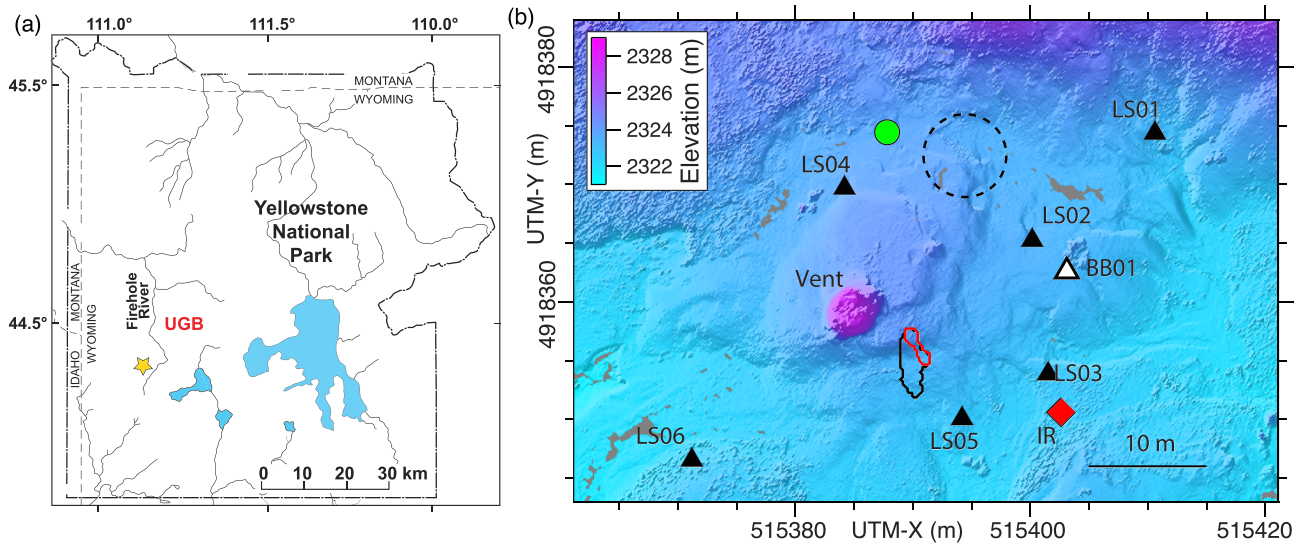
Figure 1. (a) Map of Yellowstone National Park, showing the location of the Upper Geyser Basin (UGB) and Lone Star Geyser (yellow star). (b) Map showing Lone Star Geyser vent, locations of the seismic stations (black triangles), and the infrared (IR) sensor (red diamond). The red and black polygons are the outlines of the average source volume for type-1 preplay tremor and tremor at the beginning of the main eruption, respectively (section 2.2). The black dashed circle is the approximate location of the "bubble trap" inferred by Vandemeulebrouck et al. (2014) based on the intersection of observed tremor backazimuths in the 2010 data with the local thermal pool trend (from Figure 1b in Vandemeulebrouck et al., 2014). The white triangle (BB01) is the location of the seismometer used in the 2010 experiment. The green circle is the location of a pool in which the water level oscillates with a period of ~72 s. Coordinates are in the Universal Transverse Mercator (UTM) system, Zone 12.

only at the beginning of the eruption cycle. Data from a more recent array of seismometers deployed around OFG reveal a much larger offset reservoir and tremor sources that extend still deeper (Wu et al., 2017, 2019). The data also document a systematic upward and downward migration of tremor leading up to, and following eruptions (Wu et al., 2019). Conceptually similar reservoir-conduit geometries have been inferred through downhole visual observations (e.g., Belousov et al., 2013) and from long-period ground deformation recorded by broadband seismometers (Ardid et al., 2019) and tiltmeters (Munoz-Saez, Namiki, et al., 2015; Rudolph et al., 2012).

Here we use seismic signals recorded for 4 days by multiple broadband seismometers around Lone Star Geyser (LSG), Yellowstone National Park (Figure 1), to improve the understanding of multiphase fluid storage and transport, before, during and after eruptions. We build on previous geophysical investigations at LSG (Karlstrom et al., 2013; Namiki et al., 2016; Vandemeulebrouck et al., 2014). These studies revealed complex eruption cycles in which the main eruptions that occur every ~3 hr are preceded by a variable number of preplay episodes. The eruption cycles at LSG discharge ~21 m^3 of water and form eruption columns that are ~8–12 m high (Karlstrom et al., 2013). Based on observations from a single broadband seismometer, Karlstrom et al. (2013) inferred that the main eruption is followed by a relaxation period in which acoustic emissions and the absence of water discharge indicate that the subsurface liquid continues to heat and boil while the vent is empty. Strong hydrothermal tremor was observed during the preplay episodes and at the beginning of the main eruption along with lower amplitude tremor during the relaxation period (Vandemeulebrouck et al., 2014).

The overarching goal of our study was to provide new quantitative insights on the fluid and thermodynamic processes controlling periodic geyser eruptions. The specific objectives are to (1) characterize the temporal patterns of hydrothermal tremor, (2) illuminate the geyser conduit from tremor source locations, (3) analyze the acoustic properties of preplays and explore their role in the eruption cycle, and (4) interpret the tremor patterns in terms of subsurface thermodynamic conditions and dynamics. To accomplish these goals, five broadband seismometers (Nanometrics Trillium P/PA sensors with a corner frequency of 120 s; data recorded by Tauras digitizers at 250 Hz sampling rate) were deployed at distances of ~9 to ~30 m from the geyser cone (Figure 1 and supporting information Text S1 and Figures S1–S4) between 14 and 17 April
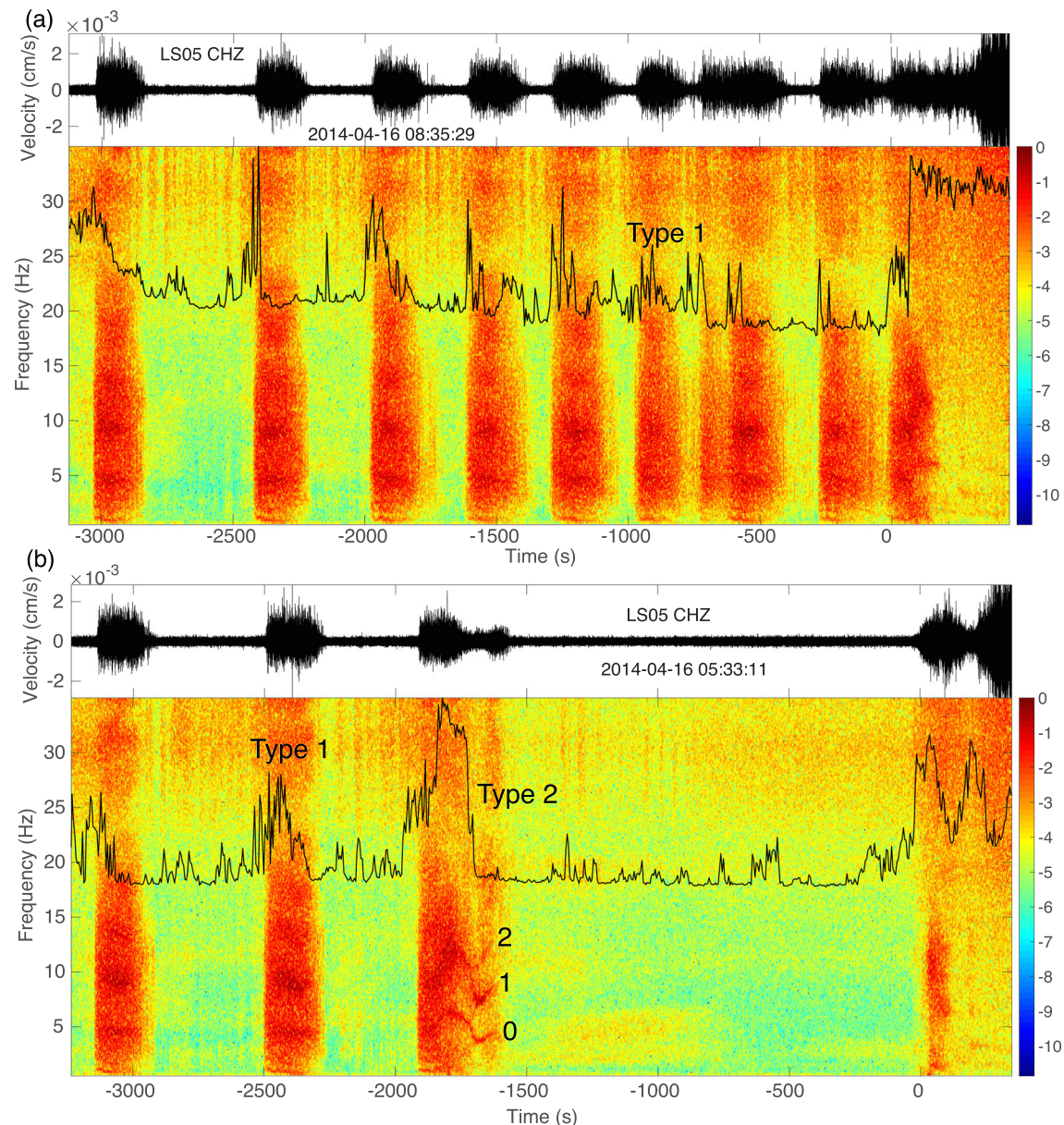
Figure 2. (a and b) Vertical component seismic records from station LS05 (Figure 1) and their spectrograms for preplays from two different eruption cycles. The upper panels show high-pass filtered (at 0.5 Hz) tremor records, and the bottom panels show spectrograms of the seismic record overlain by the IR record in arbitrary units (black trace). Spectrogram amplitudes are on a log scale. The eruption cycle in (a) has more preplays compared with the cycle shown in (b). The two types of preplays are indicated. Numbers 0, 1, and 2 on the spectrogram in (b) mark spectral peaks corresponding to the fundamental frequency, first overtone and the second overtone in the type-2 preplay. Time $t = 0$ is the onset of the main eruption (UTC time stamp is indicated on the upper panels). An image with more detail on the preplay tremor shown in (b) is provided in supporting information Figure S6. The spectrograms are calculated with Fourier transforms of 8.2-s long sliding time windows with 80% overlap.

2014. An infrared (IR) sensor directed toward the geyser vent was used as a proxy for liquid and steam discharge (Namiki et al., 2016).

2. Hydrothermal Tremor

2.1. Temporal Patterns and Characteristics

Preplay episodes at LSG display a bimodal distribution in which some eruption cycles have fewer numbers of preplays compared with others (Karlstrom et al., 2013; Namiki et al., 2016). This preplay variability is also

reflected in the temporal patterns of hydrothermal tremor (Figure 2). The eruption cycle shown in Figure 2a has eight preplay tremor episodes, whereas the one shown in Figure 2b has only three preplay tremor episodes (also shown in Figure S6; Figure S5 shows a spectrogram for an entire eruption cycle). The last preplay episode shown in Figure 2b is of significantly longer duration (~2 times) compared with other preplay episodes. We refer to these longer duration preplays as type-2 preplays, whereas the more abundant and shorter preplays are termed type-1 preplays. We recorded 29 eruption cycles with clean seismic records of which 16 have type-1 preplays only and 13 have type-2 preplays. The average durations of type-1 and type-2 preplay tremor episodes are ~200 and ~300 s, respectively. At LSG, hydrothermal tremor signals are composed of discrete short-duration impulsive seismic events that tend to merge (Figure 2 in Vandemeulebrouck et al., 2014). While the tremor amplitudes are steady for ~160–180 s, we observe hints of multiple broad spectral peaks at ~5, ~9, and ~14 Hz in type-1 preplays (Figure 2a). Type 2 preplay tremor begins similar to a type-1 preplay, but after a short period with steady amplitudes, tremor continues with lower amplitudes for an extended duration. Toward the end of the type-2 preplays, there is a clear gliding of the harmonic tremor with the regularly spaced spectral peaks. Assuming the beginning of the type-2 preplay tremor episode is at time $t = 0$, the fundamental frequency first increases slightly from ~5 Hz at $t \sim 60$ s to ~6 Hz at $t \sim 110$ s then decreases from ~6 Hz at $t \sim 170$ s to ~3.5 Hz at $t \sim 230$ s and then slowly increases to ~4 Hz at $t \sim 290$ s. Harmonic tremor is characterized by periodic repetition of a discrete seismic signal at time interval (dt), leading to evenly spaced spectral peaks with the lowest spectral peak and the spacing between the spectral peaks equal to $1/dt$ (e.g., Hellweg, 2000; Johnson & Lees, 2000; Lesage et al., 2006; Powell & Neuberg, 2003). In Figure 2b, the first overtone at frequencies that are two times the fundamental frequencies shows similar changes. The second overtone is only observed toward the end of the tremor episode. Gliding harmonic tremor also occurs during the main eruption (supporting information Text S2 and Figure S7). From the initiation of the main eruption tremor (time $t = 0$), the tremor characteristics look very similar to that of type-2 preplay tremor for the first ~150 s with slow increase in the fundamental frequency from ~5 to ~6 Hz (Figure S8). The spectral peaks are weakened and disappear between $t \sim 150$ s and $t \sim 350$ s. Thereafter, the fundamental frequency follows a smooth decreasing trend to ~2.5 Hz at $t \sim 500$ s, remains steady for most of the main eruption at ~2.5 Hz until $t \sim 1,600$ s, and then gradually increases to ~4 Hz over the next ~400 s during the relaxation tremor (Figure S7). The first overtone changes proportionally to the fundamental frequency. The tremor features described above are observed at multiple sensors (Figures S6 and S7). We also reanalyzed data that was collected at LSG in 2010 with a single broadband instrument (Vandemeulebrouck et al., 2014) and confirmed the presence of these tremor features. However, we observe more variability in the preplay sequences in the 2010 data compared with this study (supporting information Text S2). The discrete seismic events constituting the tremor signals at LSG are of similar amplitudes (~2×10^{-3} cm/s), duration (~0.5 s), and dominant frequency content (~10–40 Hz) compared to those recorded at OFG at similar distances from the geyser cone (Kedar et al., 1996, 1998; Kieffer, 1989).

2.2. Tremor Locations

We locate the source of hydrothermal tremor during preplay episodes, the beginning of the main eruption, and during the relaxation phase using the complex polarization analysis (Vidale, 1986). The methodology of extracting polarization characteristics from waveform data is explained in detail in the supporting information Text S3. Figures S9 and S10 show examples of polarization results at the two good stations LS03 and LS05, respectively (Figure 1). The polarization is characterized by the degree of polarization, the degree of linearity, and the strike and dip of the polarization direction over an eruption cycle.

To locate the tremor sources, we assume a grid of possible locations around the geyser cone. For each time window we systematically find the source location on the grid that minimizes the L1 norm of differences between predicted and the observed polarization in 4.8-s long moving time windows. We assume radial polarization, that is, P waves, which we assume to be reasonable for seismic sources in a fluid-dominated system. As we will show later, polarization directions of tremor at multiple stations are directed to a common region, and the degree of linearity is high ($\gtrsim 0.75$ for LS03 and LS05, and $\gtrsim 0.5$ for other stations), justifying this assumption. The tremor amplitudes vary substantially over the eruption cycle leading to large variation in signal-to-noise ratio (SNR). Therefore, we adopt different strategies for different periods of the eruption cycle. Polarization and location for episodes of type-1 preplay tremor and tremor at the beginning of the main eruption were calculated independently. However, tremor amplitudes toward the end of type-2

preplays and during main eruption and relaxation phase are substantially lower. Therefore, we average the covariance matrices over multiple eruption cycles following the approach of Jurkevics (1988) who similarly stacked covariance matrices over multiple stations in an array to improve the SNR. We calculate tremor locations from polarizations estimated from the average covariance matrices. Further technical details are provided in the supporting information Text S4.

Figures 3a–3c show polarization directions and the best fitting locations color coded by lapse time through a type-1 preplay tremor episode. The polarization directions at all stations appear to be radially directed toward a location ~5 m east-southeast of the geyser cone at a depth of ~7–10 m. The polarization directions and tremor locations are very stable through the tremor episode, and the locations are consistent with the polarization directions observed during preplays in the 2010 experiment (Vandemeulebrouck et al., 2014). The misfit for these locations is generally ~15°–25°. Figures 3d–3f show the best fitting tremor locations during nine type-1 preplay tremor episodes in an eruption cycle. The polarizations and tremor locations appear to be constant as the eruption progresses through the preplays.

Polarization analysis results for tremor at the beginning of the main eruption show that unlike type-1 preplays, systematic and coherent change in the strike (anticlockwise at four stations) and dip of the polarization directions (decrease in dip at LS03 and LS05) indicates a systematic change in tremor source location (Figures 4a–4c). The tremor locations are inferred to migrate southward by ~5 m and to a shallower depth of ~5 m from an initial depth of ~9 m. The shallow location is laterally offset by ~8 m toward the south-southeast of the vent (Figure 1). Determination of this offset is not robust and might result from an artifact of the recording geometry, poor coupling of the sensors with the ground, or from the heterogeneous three-dimensional seismic velocity structure that is not accounted for in the analysis. While there are uncertainties in the tremor locations, the unambiguous and systematic change in the strike and dip of the polarization indicates that the hydrothermal tremor leading toward the eruptions is fundamentally different from type-1 preplay tremor in which the polarizations are time invariant (Figure S12). As an example, Figure S13 shows the spatial distribution of misfit to the observed polarization directions on the grid of possible tremor source locations for the tremor episode shown in Figure 4a. In theory, the radial polarization directions are expected to intersect at the correct source location only if the medium is a whole-space and the seismic waves are pure *P* waves. Free-surface effects, assumption of a uniform velocity model, not accounting for the effects of subsurface 3-D structure and contamination of first-arriving *P* waves by scattered waves can lead to deviation of the actual polarization directions from a purely radial polarization. Because we assign greater weights to measurements at stations LS03 and LS05, the estimated locations primarily correspond to the polarization directions at these two stations (Figure S12).

Using polarization measurements and tremor locations over multiple eruption cycles, we calculated average volumes of tremor source locations as a function of time for both type-1 preplays and tremor at the beginning of the main eruption (supporting information Text S4). Tremor locations do not vary systematically during the type-1 preplay and are contained within a compact volume with a maximum vertical dimension of ~3 m between ~7 and 10 m below the ground surface (insets in Figures 3b and 3c). The slight elongation of the volume toward station LS05 is caused by its greater weight in the tremor location procedure compared to other stations. The results clearly indicate tremor sources migrating to shallower depths at the beginning of the main eruption in a narrow volume (insets in Figures 4b and 4c).

Out of the 13 eruption cycles for which we were able to calculate meaningful locations, only 5 had type-2 preplays. Out of the 5, only 2 show reliable tremor polarizations consistent with each other, and the rest show greater scatter in polarization directions. The polarizations and locations calculated for the average covariance matrices of the two best episodes of type-2 preplay tremor are shown in Figures 4d–4f. There is a small systematic migration of locations with time, clearly different from stable and invariant nature of tremor locations during type-1 preplay. The locations appear to migrate southward by ~2 m and shallower by ~1~2 m before moving back to the original depths around ~200 s into the tremor episode. This change is much smaller than the clear migration of locations at the beginning of the main eruption, ~5 m toward south and to shallower depths, from ~9 m to ~5 m. There is considerable uncertainty in the locations for type-2 preplays toward the end of the tremor episode because of small amplitudes.

Subsequent to the tremor source locations migrating closer to the ground surface at the beginning of the main eruption, the tremor polarization becomes chaotic but stabilizes ~5 min into the main eruption
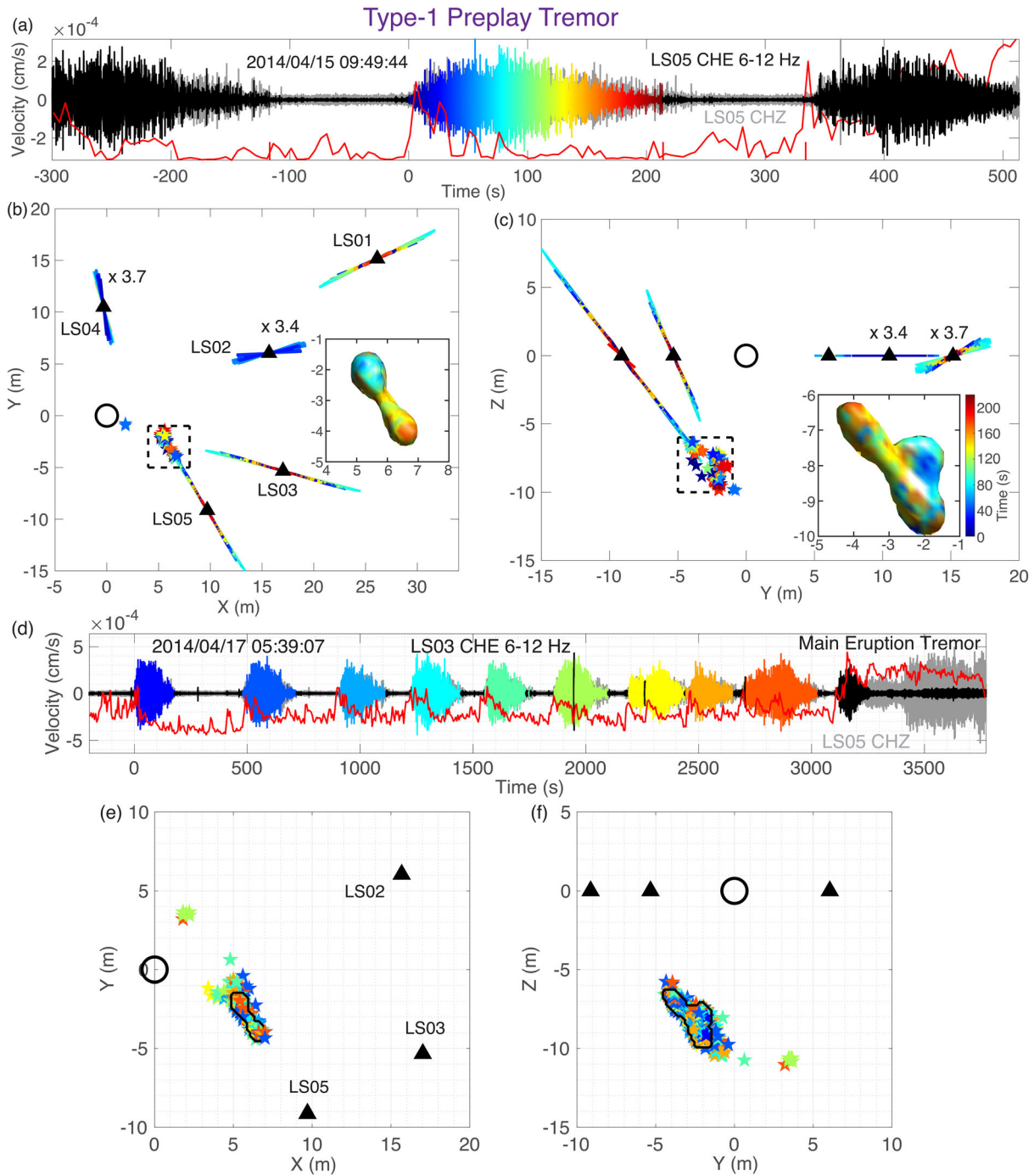
Figure 3. Tremor polarization directions and migration of tremor sources during type-1 preplays. (a) Type-1 preplay tremor record on the east-west component of station LS05 (black) filtered at 6–12 Hz with the vertical component at the same station in gray. The tremor episode is color coded by lapse time from the beginning. Red trace is the IR intensity signal in arbitrary units. (b and c) Polarization directions (lines through the stations) and best fitting locations (stars) in XY and YZ planes, respectively. Both the locations and lines are color coded according to lapse time in (a). The black circle represents the geyser vent placed at $X = 0$, $Y = 0$. The dashed black rectangle in (b) and (c) delineates the area shown in the insets. The insets in (b) and (c) show the average volume containing tremor source locations for type-1 preplay tremor, color coded by lapse time. The timescale is shown next to the inset in (c). Positive X, Y, Z directions point to east, north, and up. (d) Similar to (a) but showing tremor record for all type-1 preplays in an eruption cycle on the EW component of LS03 (black) filtered at 6–12 Hz. Polarization and location analysis is performed on all type-1 preplay tremor episodes, which are assigned separate colors. (e) and (f) Best fitting tremor locations (stars) in XY and YZ planes, respectively, color coded by preplay tremor episode. The black polygon in (e) and (f) outlines the average source volume for type-1 preplay tremor shown in the insets in (b) and (c).
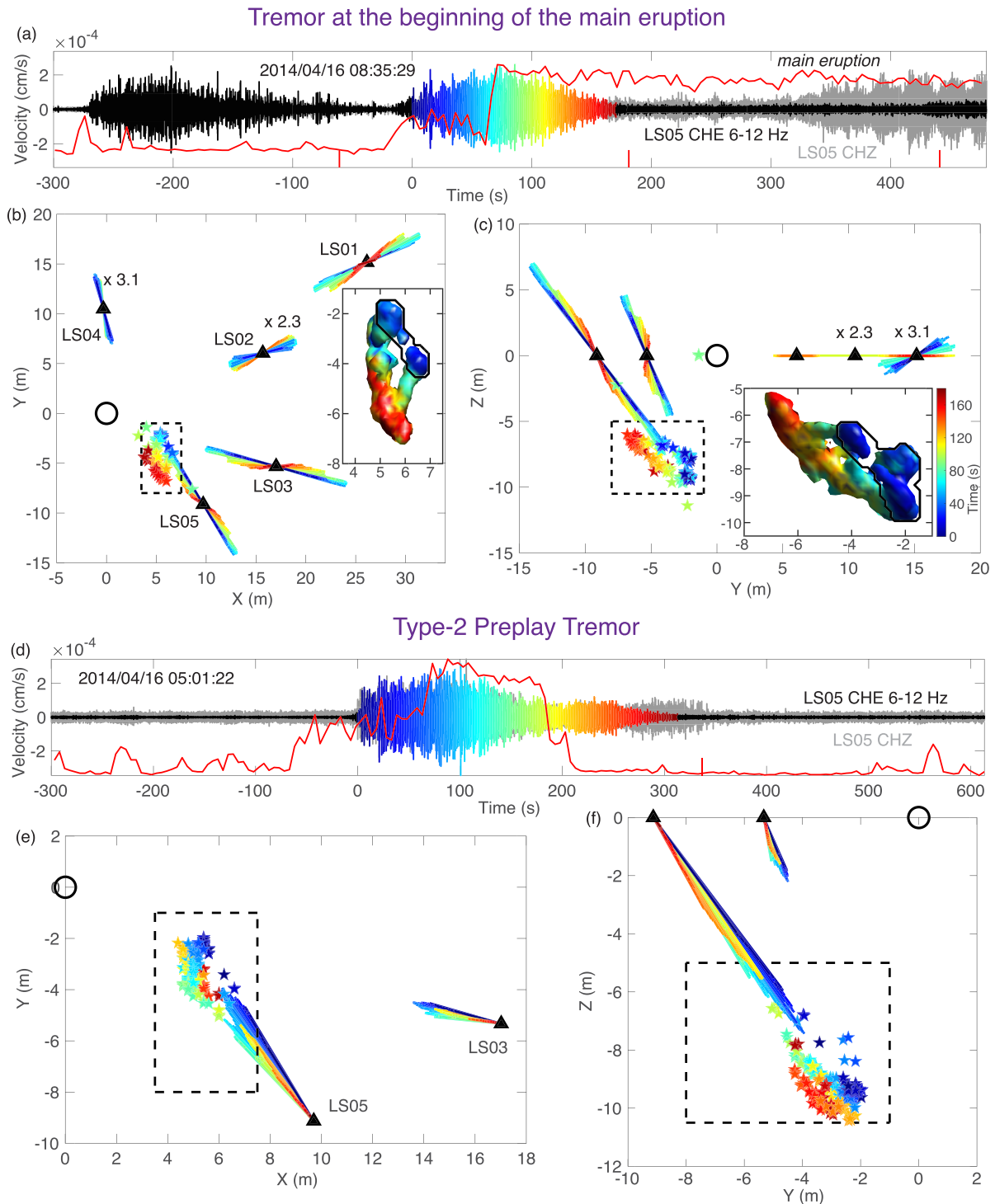
Figure 4. (a–c) Similar to Figures 3a–3c, respectively, but for tremor episode at the beginning of a main eruption (note the sustained peak in infrared record and large-amplitude high-frequency signals on the vertical component). The black polygon in insets in (b) and (c) outlines the average source volume for type-1 preplay tremor shown in the insets in Figures 3b and 3c, reproduced for better comparison. (d–f) Similar to Figures 4a–4c, respectively, but for type-2 preplay tremor. The dashed black rectangle in (e) and (f) delineates the area shown in the insets in (b) and (c), reproduced for better comparison. The locations are actually calculated for polarizations averaged over two tremor episodes. The tremor record in (d) is provided as a reference for time.
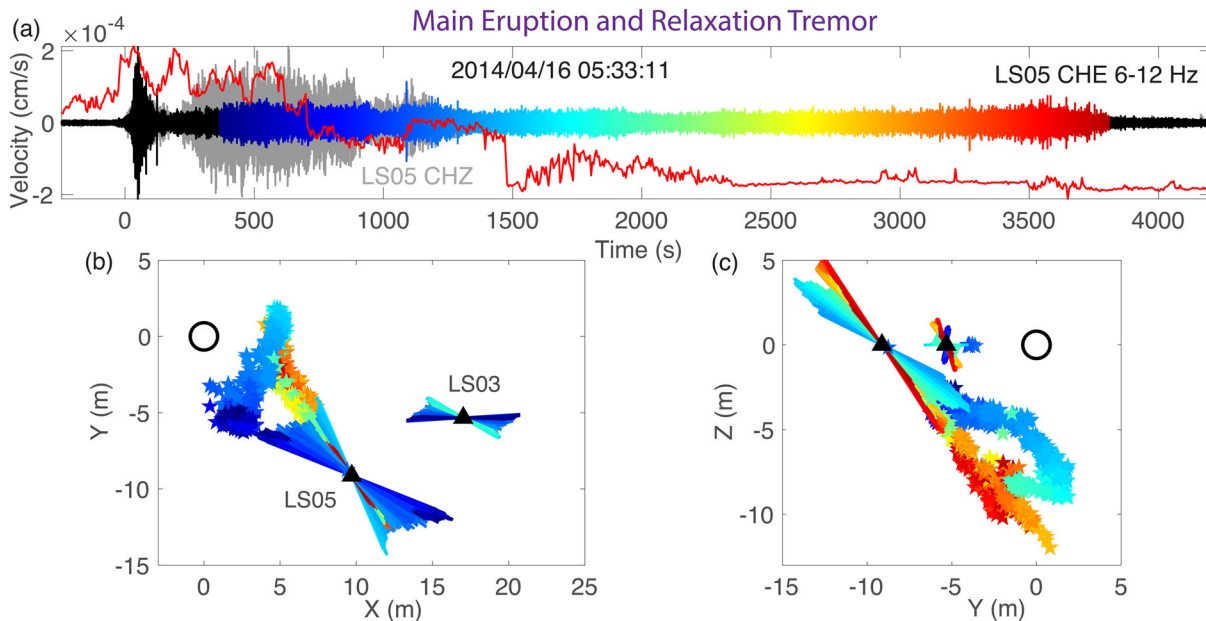
Figure 5. (a–c) Similar to Figures 4d–4f, respectively, but for tremor during the main eruption and in the relaxation phase.

(Figures S9 and S10). The tremor source locations are stable and concentrated at a depth of ~4 m through the duration of relatively greater high frequency amplitudes on the vertical components (Figure 5). Subsequently, the source locations slowly migrate to slightly greater depth in a north-northeast direction over ~500 s, before rapidly moving to greater depths over the next ~700 s (evident from the increase in dip angle at LS05, Figure S10). This path appears to be similar to the path of rapid tremor source migration at the beginning of the main eruption but in the opposite direction, and occurs over a much longer time period. The differences in paths could be caused by the smaller number of stations used for this analysis (only LS03 and LS05). The locations finally stabilize at depths of ~7–11 m until the end of the relaxation period, very close to the source locations of type-1 preplays.

We also checked the results of using shorter (3.6 s) and longer time windows (9.6 s) for calculating source locations for type-1 preplay tremor and tremor at the beginning of main eruptions. The polarizations are mostly similar (Figure S14) with lower variability for the longer time window, because averaging over a longer time reduces noise in the polarization measurement. The resulting average tremor source volumes are largely unchanged (Figures S15 and S16). Our tremor source locations critically depend on the two good stations, LS03 and LS05. We also tested the effect of removing one of these stations on tremor source locations (Figures S17 and S18). Removal of one of these stations leads to a systematic shift and greater scatter in the tremor locations in both cases. However, the pattern of temporal change in tremor locations is similar. The locations are stable during type-1 preplays. During the tremor episode at the beginning of the main eruption, tremor locations migrate southward and shallower. However, locations calculated using LS05 show a greater change in depth compared to locations calculated using LS03. Using stations LS03 and LS05 only for calculating tremor source locations does not change the results substantially because quality weights for these stations in location procedure are already greater than weights for other stations.

2.3. Variation in Preplay Sequences

We study the effect of the two types of preplay sequences (Figure 2) on the main eruption. The main eruption at LSG is characterized by a tall eruption column, and the eruption interval has been stable at approximately ~3 hr since at least 1920 (Karlstrom et al., 2013), which was also observed during the 2010 experiment (Vandemeulebrouck et al., 2014) and during the 2014 experiment. We examine the time difference between the end of the last preplay and the onset of the main eruption for the two types of eruption cycles (Figures 6a and 6b). Excluding a few outliers, the two types of preplay distributions appear well separated from each other in data collected in both the 2010 and 2014 experiments. In eruption cycles with a large number of
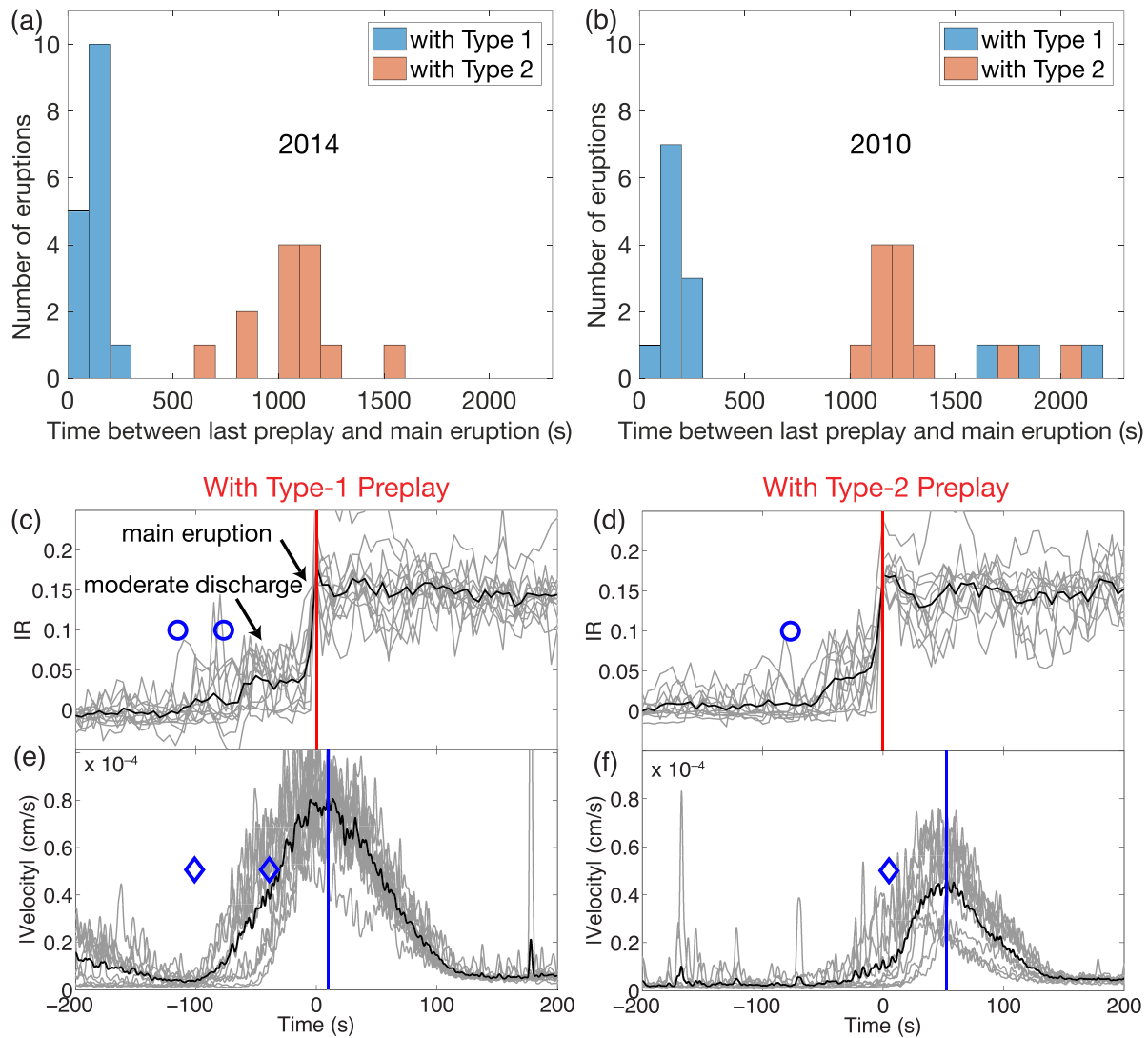
Figure 6. (a and b) Histograms of the time difference between the end of the last preplay and the onset of main eruption for the two types of eruption cycles (Figure 2) for (a) data collected in 2014 and (b) data collected in 2010 (Vandemeulebrouck et al., 2014). Bin width is 100 s. (c) Infrared signals (arbitrary scale) aligned at the onset time of the main eruption and formation of a tall fountain (red vertical line at $t = 0$) of eruption cycles with large number of type-1 preplays. The blue circles are visually confirmed (by camera recordings) initiation times of moderate discharge before the main eruptions for two cycles. (e) Tremor amplitudes filtered (6–12 Hz) and smoothed over 4 s sliding windows for the same eruptions. The blue diamonds are tremor onset times for the specific eruption cycles marked by blue circles in the upper plot. (d and f) Same as (c) and (e), respectively, but for eruption cycles with type-2 preplays.

preplays the main eruption follows the last preplay within ~2–3 min. In eruption cycles with a type-2 preplay, the main eruption is significantly delayed, by ~18–19 min on average, with respect to the preplay (e.g., in Figure 2b). We find that the preplay sequence impacts not only the time of the main eruption but also its onset process. The main eruption is preceded by moderate discharge or overtopping of water, similar to that seen during type-1 preplays, that last for ~70 s (Figure S19). Figures 6c and 6e show infrared signals and the tremor amplitudes at the beginning of main eruption for multiple eruption cycles with a large number of type-1 preplays. The tremor generally begins after the moderate water discharge leading to the main eruption (small increase in infrared intensity at $t \sim -60$ s) but before development of the main eruption column (indicated by the infrared peak at $t = 0$), following which, the tremor amplitudes decrease (Figure 6e). For eruption cycles with a type-2 preplay, the onset and amplitude maximum of tremor at the beginning of the main eruption are delayed by ~50 s with respect to the infrared signals, the tremor amplitudes are much lower, and the duration of the tremor episode is shorter by ~40–50 s (Figures 6d and 6f).

The eruption cycles used to calculate the average source volume for tremor at the beginning of the main eruption (insets in Figures 4b and 4c) are primarily the ones that contain a large number of type-1 preplays, selected because of greater amplitudes and better SNR. We also attempted to calculate equivalent tremor source locations for eruption cycles with type-2 preplays separately. The covariance matrices for tremor during five eruption cycles were averaged to estimate average polarizations and source locations (Figure S20). The tremor locations migrate toward the south and to shallower depths, by ~4 and ~2 m, respectively, over ~100 s. This migration is slightly smaller compared to that for eruption cycles with a large number of type-1 preplays (~5 and ~5 m, respectively in Figures 4b and 4c) that have longer tremor durations (~160 s). However, we observe greater scatter due to lower tremor amplitudes and fewer number of eruption cycles used in averaging, and it is possible that locations calculated from a greater number of eruption cycles might result in similar locations for the two types of eruption cycles. Further insights on the tremor locations at the beginning of the main eruption can be gained from examining the dip of polarization at the closest stations LS03 and LS05. There are subtle differences in the temporal pattern of dip angle for the two types of eruption cycles (Figure S21). The dip angle at both stations steadily increase for ~90–100 s before rapidly decreasing at the end of the tremor episode in eruption cycles with type-2 preplays. In contrast, for eruption cycles with large number of type-1 preplays, the dip angle at LS03 slowly starts decreasing from ~100 s, whereas dip angle at LS05 slowly increases until ~140–150 s before dip angles at both stations rapidly decrease in the last ~20–30 s. The two best recorded type-2 preplay tremor episodes (16 April 2014 05:01:22 and 17 April 2014 11:27:00) show very consistent dip trends until ~290 s (Figure S22). The evolution of tremor dip angles at both stations during the first ~140 s of type-2 preplay is remarkably similar to that for tremor at the beginning of the main eruption in eruption cycles with large number of type-1 preplays (Figures S21 and S22).

2.4. Source Mechanism of Hydrothermal Tremor

Moment tensors can help quantify source models for generating tremor (e.g., Chouet & Matoza, 2013; Jost & Herrmann, 1989). However, estimation of moment tensors requires Green's functions calculated using an appropriate subsurface seismic velocity model (Bean et al., 2008; Cesca et al., 2008; Trovato et al., 2016). Assuming the hydrothermal tremor signals at LSG are caused by fluid-related processes, an appropriate seismic velocity model of the geyser system should include a conduit containing a liquid-steam mixture along with a larger cavity and/or surrounding porous medium. There are some direct observations of the approximate shape and dimensions of geyser conduits at OFG (Hutchinson et al., 1997) and El Jefe Geyser at El Tatio, Chile (Munoz-Saez, Manga, et al., 2015), but no information exists for LSG. Calculating seismic waves for such a realistic velocity model containing solid-fluid media also requires numerical methods (e.g., Lecoulant et al., 2019), which is beyond the scope of this study given the lack of definitive knowledge on the velocity structure and high-quality dense data to validate the simulated waveforms. We therefore assume low-frequency (~2–8 Hz) waveforms and use simple 1-D velocity models to calculate a point-source moment tensor for seismic events constituting type-1 preplay tremor. A low-frequency passband was selected to justify the point source assumption and to use simple velocity models. To the best of our knowledge, this is the first attempt to estimate a seismic source mechanism for hydrothermal tremor in a geyser system. Unlike the moment tensor inversions traditionally performed in volcano seismology (e.g., Chouet & Matoza, 2013), we invert for a point source in space and time (i.e., source is an impulse or Dirac delta function in space and time) with no single force components, resulting in only six model parameters. We expect the source estimates in this study to be refined in future studies as more data become available and our knowledge of the subsurface velocity structure improves.

We estimated ~1.0-s long average representative displacement waveforms filtered at ~2–8 Hz for a randomly chosen seismic event in type-1 preplay tremor (supporting information Text S5 and Figure S23). We establish a 3-D grid of possible source locations ($X = -6$ to 11 m; $Y = -11$ to 9 m; $Z = -3$ to -80 m) encompassing the average tremor source volumes of type-1 preplay tremor and tremor at the beginning of the main eruption. The grid is extended to depths greater than that suggested by polarization analysis to evaluate the possibility of deeper tremor sources as inferred by Wu et al. (2019) at OFG. At each location, we invert for the point source moment tensor that provides the best fit to the recorded long period waveforms (Kawakatsu, 1998; Minson & Dreger, 2008; Nayak & Dreger, 2014, 2018; Tsuruoka et al., 2009). A number of studies at OFG, also located in the UGB of YNP, provide some constraints on the general seismic velocity structure near

geysers. Cros et al. (2011) assumed a layered V_S structure, with V_S increasing from ~0.1 to ~0.6 km/s over the top ~20 m. Wu et al. (2017) estimated considerably higher Rayleigh wave velocities ~1.0–1.6 km/s at frequencies ~0.5–5 Hz. Using hammer shot data collected on a line of receivers passing through OFG, Caylor (2020) estimated V_P increasing from ~1.5 km/s to ~3.2 km/s over the top ~50 m, which translates to V_S ~ 0.9–1.9 km/s, assuming V_P/V_S ratio ~1.62. To cover this wide range of V_S estimates, we test a number of uniform half-space velocity models with V_S ranging from 0.1 to 1.6 km/s. The V_P/V_S ratio is assumed to be 1.62. Green's functions were calculated using the frequency-wavenumber integration method (Wang & Herrmann, 1980) as provided in Herrmann (2013). Green's functions were filtered with the same filter as observed data (causal Butterworth) and inverted for full moment tensors at all possible locations on the 3-D source grid. The goodness-of-fit between observed and predicted waveforms is characterized by variance reduction (VR; Minson & Dreger, 2008). The grid point providing the best waveform fits between the observed and predicted waveforms (VR$_{MAX}$, maximum VR) for the inverted moment tensor is inferred to be the centroid location, and the corresponding moment tensor is inferred to be the most appropriate for the seismic event. We tested inversions both with and without inverse sum-of-squares weights applied to each station that lead to nearly equal weight to each station in the inversion, irrespective of the amplitudes. We decompose all moment tensors into a combination of isotropic (ISO), double couple (DC) and compensated linear vector dipole (CLVD) moment tensors, assuming the same principal stress orientations for DC and CLVD moment tensors (Jost & Herrmann, 1989).

Using station LS01, which is twice the distance as other stations from the geyser, allows us to constrain the effective subsurface velocities at LSG. Even at low frequencies (~2–8 Hz), models with very low velocities V_S ~0.1–0.4 km/s lead to a pronounced lag in synthetic waveforms at LS01 (Figure S24). This is unlike the observed waveforms that are approximately uniform in phase at all stations. Waveform fits at LS01 with respect to other stations and the overall waveform fits gradually improve with V_S increasing up to ~0.8 km/s, followed by a very small decrease with further V_S increase (Figure S25). The best moment tensor contains ~44% positive ISO moment and ~38% CLVD moment and fits observed waveforms at VR$_{MAX}$ ~85.3% for our preferred model with V_S ~0.8 km/s (Figure 7a). The best fitting location is right under the geyser cone at a depth of 10 m (Figures 7b and 7c). In order to assess the uncertainties in the centroid location and the moment tensor, we estimate a threshold VR (VR$_{TH}$) above which all locations and moment tensors are treated as probable solutions. Depth-dependent and VR$_{MAX}$-dependent values of VR$_{TH}$ are statistically estimated from moment tensor inversion of a large number of realizations of synthetic waveforms contaminated with real observed noise following the approach of Nayak and Dreger (2018) modified from Almendros and Chouet (2003). The probable source volume containing all locations with VR > (VR$_{TH}$ ~ 84.1%) extends from a depth of ~7 to ~15 m over an area with a radius of a few meters centered at the geyser (Figures 7b and 7c). The best fitting depths and the region of well fitting locations are generally similar and restricted to depths ≲20 m for all models with V_S ≳ 0.6 km/s and the average 1-D model from Caylor (2020). The source depths derived from the moment tensor analysis are slightly deeper than the depths estimated from polarization analysis (~5–10 m), because of the lower frequencies in the moment tensor analysis (~2–8 Hz) compared with the polarization analysis (~6–12 Hz). Essentially, the centroid location and the moment tensor are inferred from a smoothed version of the actual wavefield used in the polarization analysis. In order to assess the uncertainty in the moment tensor solutions in the source-type space, we calculate the composite network sensitivity solution following the methods of Nayak and Dreger (2015) and Nayak and Dreger (2018). The region of the best fitting source types (VR > 84.1%) in the composite network sensitivity solution covers a wide range of moment tensor solutions with positive isotropic moments (~3%–71%) and CLVD moments (~0%–90%) as seen in the Hudson source type plot (Hudson et al., 1989; Figure 7d). The large uncertainty in source type is essentially caused by absence of stations over a wide range of azimuth (azimuthal gap of ~210°) to the west of the geyser. The relative lack of energy on the tangential components and the uniform nature of the dominant radial and vertical component waveforms at all stations favor a non-double-couple source (Figures 7a and 7d). Purely isotropic sources result in poorer waveform fits, indicating some nonisotropic radiation at the source or an equivalent effect due to the 3-D structure or a fluid-solid interface in the source region that is not accounted for in simple velocity models. Incorporating a parabolic source-time function of width ~0.03 s, similar to the width of pressure pulses observed at OFG (Kedar et al., 1998), does not significantly improve the quality of waveform fits.
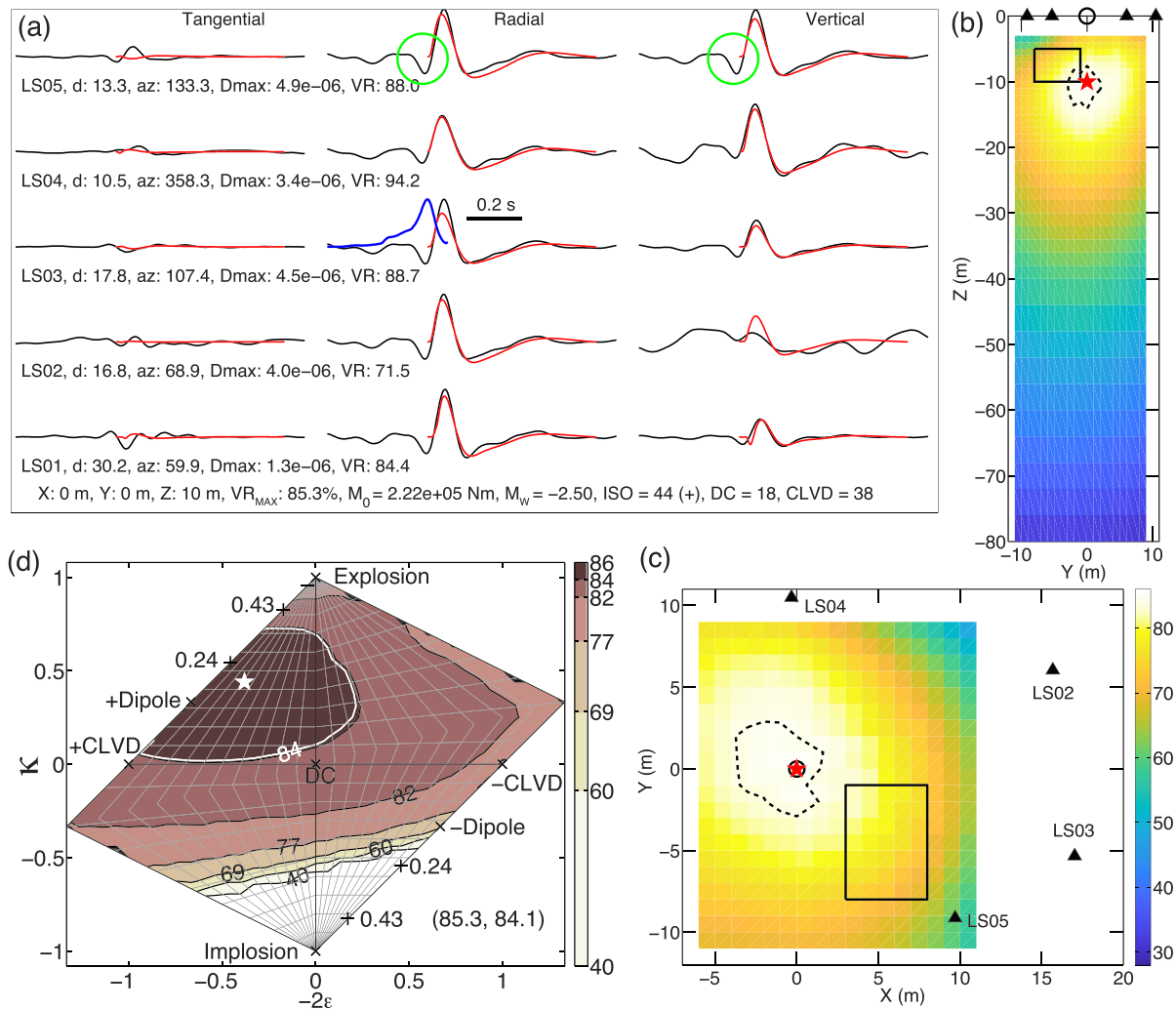
Figure 7. (a) Waveform fits corresponding to the best fitting moment tensor solution and centroid location of a representative seismic event constituting the hydrothermal tremor. The Green's functions are calculated assuming a uniform half-space with V_S 0.8 km/s. Black and red traces are observed and predicted displacement waveforms (2–8 Hz). Variables d and az are distance (m) and azimuth (°) to the stations. D_{max} is peak displacement amplitude (cm). ISO, DC, and CLVD are percentage of isotropic, double-couple, and compensated linear vector dipole moments in the solution. Goodness of fit to the waveforms is indicated by VR_{MAX}. The blue trace shows the best VR versus origin time. The peak of the blue trace corresponds to the inferred origin time (beginning of the red trace). The green circles highlight the initial negative phase in the waveforms that is not fit by any of the half-space velocity models. (b and c) Spatial distribution of VR (color map) on the source grid on the YZ and XY planes, respectively, through the best fitting location (red star). Black triangles are the stations, and black circle is the surface location of the vent. Black polygon is the region of tremor source locations from polarization analysis (Figures 4a–4c). Black dashed polygon is the probable source volume, that is, volume containing grid points that provide similar level of goodness of fit to the data, corresponding to VR > 84.1%. (d) The composite network sensitivity solution showing VR on the source-type space. Black crosses are the positions of major theoretical source types. Black "+" signs are positions of crack source types with corresponding values of Poisson's ratio indicated next to the signs. The white contour corresponds to the region of the best fitting source types (VR > 84.1%), and white star corresponds to the source type of the best fitting moment tensor.

Our results have a major shortcoming in that all of our simple half-space models fail to fit the initial negative half cycle observed in the radial and vertical component waveforms (Figure 7a). This is despite fitting the later segment of the waveforms well at VR > 80%. It is possible that our moment tensor is a cycle-shifted solution (origin time delay ~0.07 s) resulting from a simplified velocity model and the actual ISO component is negative. It is also possible that the actual seismic source is of a finite duration and our moment tensor, assumed to be a point source in time, only captures the later, more dominant volume-increase phase of the source. The source mechanism for the initial smaller energy release could be different. The compressed steam in a collapsing bubble generates an impulsive high-pressure wave (Rayleigh, 1917). Assuming a uniform medium, a volume-increase seismic source should lead to positive radial displacements, negative

traction, and hence positive pressure, which is consistent with the positive pressure signals recorded by the pressure sensor in the OFG conduit (Kedar et al., 1996, 1998). Cavitation, or bubble collapse, produces an impulse with a pressure increase in the surrounding fluid (e.g., Ceccio & Brennan, 1991), consistent with a volume-increase moment tensor. Forward modeling of waveforms (not shown here) suggests that a layer of very slow material ($V_S < 50$ m/s) at the source location can possibly generate the initial negative cycle seen in the observed data. However, at such low velocities in the source region, waveforms and the resulting moment tensors become extremely sensitive to the value of V_S leading to large variability in the resulting moment tensor solutions. Wu et al. (2017) observed pronounced group delays in empirical Green's functions derived from ambient noise cross correlation across an area southwest of OFG. They infer a large fractured and porous reservoir (lateral dimensions ~200 m, depth extent ~10–60 m) with velocities reduced by as much as ~70% (Rayleigh wave group velocity ~0.33 km/s at ~7.5 Hz). However, they interpret the depth extent of the Rayleigh wave sensitivity kernels as the depth extent of the anomaly which could be smaller if the anomaly was stronger. The absence of time delay in the waveforms at station LS01 with respect to waveforms at the other stations closer to LSG as seen in the synthetic waveforms for the slower velocity models (Figures S24 and S25 and 7a) rules out such a large region of pronounced low velocities ($V_S < 600$ m/s) in the top ~80 m at LSG. For $V_S \sim 800$ m/s and dominant period of ~0.25 s (frequency ~4 Hz), our wavelengths are ~200 m, significantly greater than the source-receiver distances in our study area. In the absence of a dense large-aperture network of receivers, we are unable to place more constraints on the dimensions of a low-velocity body.

While using low-frequency waveforms can reduce the impact of errors from wave propagation effects due to the unaccounted 3-D velocity structure, accurate determination of the source mechanism as modeled by the moment tensor critically depends on the elastic parameters in the source region (Nayak & Dreger, 2018; Vavrycuk, 2013; Zhu & Ben-Zion, 2013). To verify this at LSG, we assume that the seismic events at LSG are caused by bubble collapse and calculate the first-order estimate of the pressure change associated with these events from the scalar seismic moment (M_0). For an isotropic source, the M_0 can be related to source properties such as pressure, volume, and radius of the source. In the composite network sensitivity solution, for all solutions with VR > 84.1% and large isotropic moments (ISO > 65%), $M_0 \sim (1.9–2.2) \times 10^5$ Nm. Kumagai et al. (2014) reviewed relations among seismic scalar moment, volume, and pressure for multiple source models. For isotropic seismic sources, $M_0 = (\lambda + 2\mu)\Delta V_s$ in which λ and μ are Lame's parameters and ΔV_s is the volume change. ΔV_s can be related to two different pressure parameters: $\Delta V_s = \dfrac{\pi R^3 \Delta P}{\mu}$ and $\Delta V_s = \dfrac{4\pi R^3 \delta P}{3(\lambda + 2\mu)}$ for a spherical source model and strain-free stress in an Eshelby spherical source model, respectively (Kumagai et al., 2014). R is the radius of the seismic source, δP is the applied pressure, and ΔP is the pressure after the equilibrium state (Kumagai et al., 2014). Assuming a bubble radius of ~0.05 m as inferred by Kedar et al. (1998), we obtain $\Delta P \sim (1–3) \times 10^8$ and $\delta P \sim (3–5) \times 10^8$ for the source in our uniform half space model of $V_S \sim 0.8$ km/s. These values are significantly greater than the value of $\Delta P \sim 2 \times 10^4$ Pa directly observed by Kedar et al. (1998) in pressure recordings at OFG. The correct value will depend on the effective response and effective V_P/V_S ratio of the narrow, water-filled conduit at low frequencies as well as the bubble radius.

2.5. Harmonic Tremor

Spectrograms of seismic records at station LS03 (Figure 1) show gliding harmonic tremor, primarily in between tremor cycles (Figure 8). These signals are not obvious at any other station suggesting that the source should be shallow and localized in proximity to LS03. The harmonic tremor signals are caused by the periodic repetition of discrete high-frequency (~40 Hz) short-duration (~0.1 s) events (Figure 8 and supporting information Text S6 and Figure S26). The time intervals between discrete events constituting harmonic tremor at LS03 sometimes change smoothly or abruptly leading to shifting spectral peaks/lines; the amplitudes can change as well. The fundamental frequency in harmonic tremor during preplay is ~5 Hz (time interval between repeating events ~0.2 s), and up to two overtones (maximum ~15 Hz) are present. In contrast, the fundamental frequency in the harmonic tremor recorded at LS03 in between eruption cycles can be as low as ~0.17 s (time interval between repeating events ~6 s) and sometimes more than 20 overtones are present. The existence of so many overtones requires very high regularity for the repeating seismic events constituting the harmonic tremor with near-constant time interval (Hellweg, 2000; Hotovec et al., 2013; Powell & Neuberg, 2003). The greater time interval between the repeating seismic events and the greater
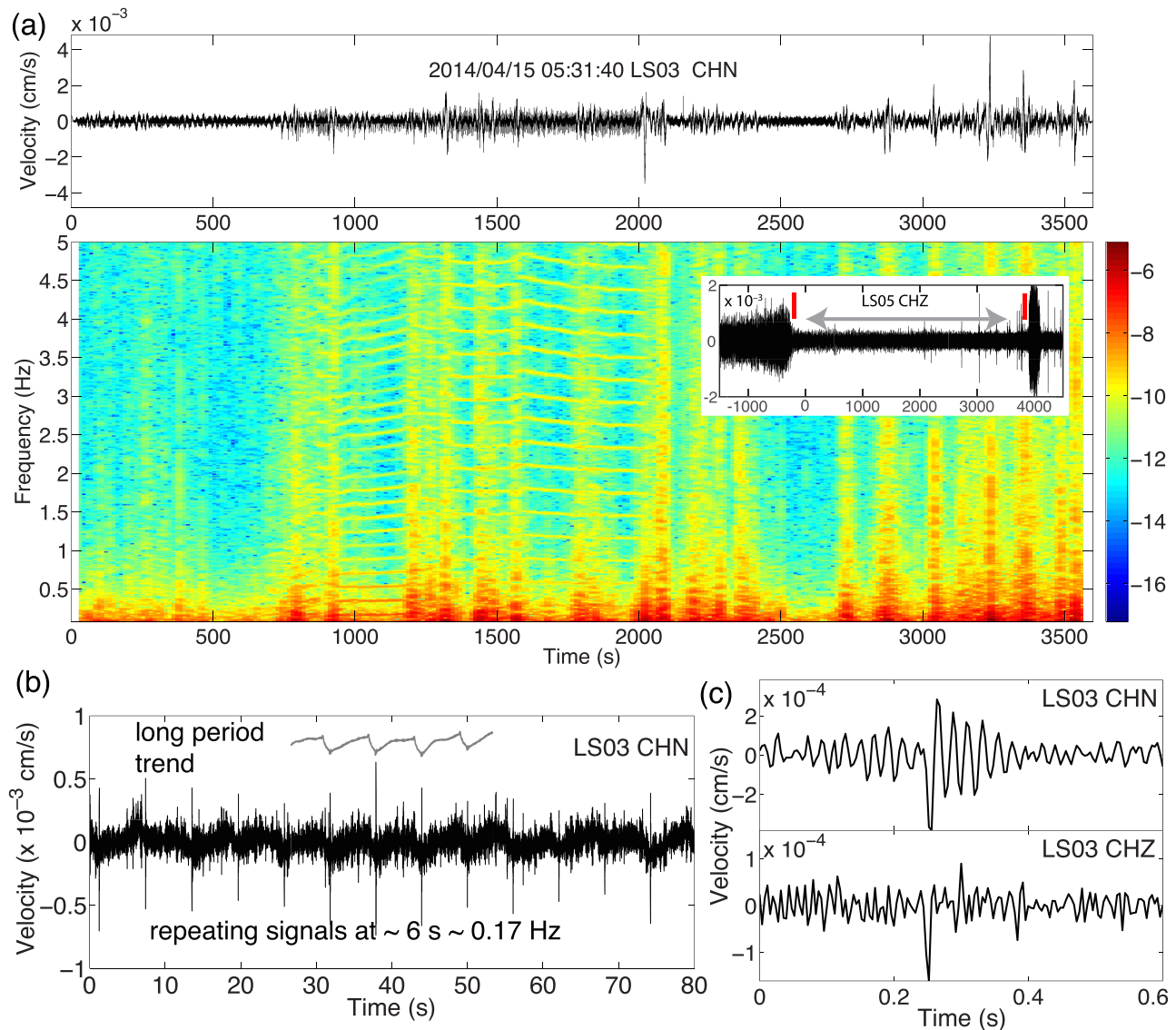
Figure 8. (a) Similar to Figure 2 but showing harmonic tremor recorded at LS03 between two eruptions cycles. This spectrogram is calculated with Fourier transforms of ~65-s long sliding time windows with 80% overlap. Inset shows the time period analyzed (gray line with arrows) in the context of a longer duration tremor record showing the end of the relaxation phase of the previous eruption cycle and the first preplay of the next eruption cycle (red ticks). (b) North-south component record at LS03 showing repeating seismic signals (interval ~6 s) constituting the harmonic tremor between eruption cycles, similar to the episode shown in (a). (c) Plot showing two components for a single randomly chosen instance of the discrete, repeating signal.

regularity of the repetition indicates a slower and more steady source process compared to that during the preplays. This is consistent with these signals being primarily observed in between the eruption cycles when the geyser is quiet and the reservoir is slowly recharged. We draw no strong conclusions from these observations as they are obvious only at one station. However, analysis of phase coherence of waveforms in the time-frequency domain at other stations suggests that these signals are likely present below the noise level at LS05 (Figure S27).

3. Discussion

The erupted liquid water and condensed steam splash on the geyser mound as water droplets. It is important to consider the possibility that the observed seismic signals are merely the signature of water droplets falling on the sinter surface. If water splashing on the geyser mound were the source of the tremor-like seismic

signals, the following would be expected: (1) seismic amplitudes during the preplays would be smaller than amplitudes during the main eruption because water discharge in the main eruption is significantly more vigorous than during preplays, (2) seismic signals would be synchronous with liquid-steam discharge as indicated by the IR record, and (3) there would be small variations in tremor polarization azimuths because the wind scatters the falling water droplets over a finite area that varies with wind direction. Our observations diverge from these expectations: (1) the tremor amplitudes in the ~6- to 12-Hz passband during the preplays are much greater than amplitudes during the main eruption, (2) there is a clear and significant time lag between onset of water discharge as indicated by IR records and onset of preplay tremor (e.g., Vandemeulebrouck et al., 2014), and the tremor continues even after the discharge and splashing on the geyser mound stops (Figures 2b and S6 and S7), and (3) the tremor polarizations are very stable and consistently point to a small area. Therefore, we conclude that the tremor-like seismic signals recorded at LSG reflect subsurface phenomena and not water splashing on the geyser mound.

We find the preplay sequences and associated hydrothermal tremor to be of two distinct types. Some eruption cycles have a larger number of shorter duration preplays (type 1), and the other eruption cycles have fewer preplays with the last preplay being of significantly longer duration (type 2). Using polarization analysis and assuming dominance of P waves, we locate the tremor sources. The discrete seismic events constituting hydrothermal tremor at LSG and OFG have been attributed to pressure impulses possibly caused by collapse of ascending steam bubbles or bubble nucleation by cavitation (Kedar et al., 1998; Vandemeulebrouck et al., 2014). At OFG it was estimated that bubbles collapse at the top of the water column in the conduit, which is the water-atmosphere interface (Kedar et al., 1998; Vandemeulebrouck et al., 2013). Evidence for this comes from seismic locations (Vandemeulebrouck et al., 2013), video observations in the top ~1 m of the water column (Hutchinson et al., 1997), and the pressure data in the water column that show that pressure pulses corresponding to seismic events reach the top pressure sensor first in the water-filled conduit (Kedar et al., 1998). Simultaneous occurrence of tremor at depth (~6–10 m) and overtopping and discharge of water at the surface during preplays suggests that tremor at LSG originates deep in the water column. However, we cannot rule out bubble collapse at shallower depths due to the limitations of our polarization-based location method. It is also possible that a narrow constriction in the conduit at depths ≲5 m prevents bubbles from migrating to shallower depths. The depth at which the bubbles collapse should theoretically vary diurnally and seasonally because it depends on the ambient air pressure (Kedar et al., 1998). However, analysis of interval between eruption records at OFG has suggested that eruption intervals are insensitive to variations in air pressure (Hurwitz et al., 2014).

Seismic signals during both types of preplays at LSG feature harmonic tremor. The temporal change in the harmonic tremor frequencies in the type-2 preplay tremor (Figure 2b) suggests that they originate from the source, rather than being path effects inferred at OFG (Kedar et al., 1998). The spectral peaks in preplay tremor at ~5, ~9, and ~14 Hz are clearly caused by periodic repetition of discrete seismic events with a time interval of ~0.2 s such that the spectral peak at ~5 Hz is the fundamental mode and the spectral peaks at ~9 and ~14 Hz are first and second overtones, respectively (Figure 2b). The temporal change of up to ~30% in the spectral peaks during the type-2 preplays implies a change from ~0.15 to ~0.3 s in the time interval between the repeating seismic events constituting the harmonic tremor. Video observations at natural geysers (Belousov et al., 2013) and laboratory geyser models (Adelstein et al., 2014; Rudolph et al., 2018) suggest the presence of "bubble traps," that is, subsurface reservoirs or large fractures that accumulate steam bubbles that are episodically released leading to eruptions. Assuming hydrothermal tremor at LSG is caused by bubble collapse, a geometrical constriction that releases steam bubbles from such a "bubble trap" at regular time intervals could explain the spectral peaks. A constriction in the conduit of LSG was inferred based on calculated choked flow conditions (Karlstrom et al., 2013). Since preplay tremor closely follows discharge of liquid water and steam at the vent, the steam bubbles are likely generated deeper in the geyser system due to steady heat flux (Vandemeulebrouck et al., 2014). As the geometrical constriction is invariant in time, there must be a change in the source or properties (such as size) of the steam bubbles to cause the gliding in frequency. A bubble cloud that can oscillate and impart energy to the walls can also explain the observed spectral peaks and gliding (Chouet, 1996; Lu et al., 1990; Yoon et al., 1991). The bubble cloud is expected to remain stable, but changes in its size or shape will modify its resonant frequency.

Other oscillatory phenomena have been observed in data collected at geysers, primarily in two separate period ranges, either tens of seconds or ~1–2 s. At OFG, oscillations of ~60 s period in the tremor source depths, amplitudes, and central frequency have been attributed to free oscillations of the water-filled column (mass) in the conduit acting on a compressible steam-rich recharge cavity that acts as a spring (Vandemeulebrouck et al., 2013). Karlstrom et al. (2013) and Vandemeulebrouck et al. (2014) report "flow oscillations" at periods ~20–70 s in IR and microphone data during various stages of the eruption cycle at LSG, explained by a similar mechanism. However, the same phenomenon has been used to explain a contrasting spectral peak at ~1 Hz (~1-s period) observed in the pressure data collected in the water column at OFG (Rudolph et al., 2018). The spectral peaks and gliding described in this study are at higher frequencies compared to those in Karlstrom et al. (2013) and Vandemeulebrouck et al. (2014) and therefore may be caused by a different process. Temperature oscillations with periods of ~30 s were observed in the OFG water column and were attributed to convective patterns (Hutchinson et al., 1997). Pressure oscillations at periods ~1–2 s in the conduit of El Jefe Geyser (El Tatio, Chile) just prior to the eruption were interpreted to result from steam bubbles entering the conduit at regular intervals (Munoz-Saez, Manga, et al., 2015). Only station LS04 (Figure 1) shows a persistent and strong intermediate frequency spectral peak at ~1.5 Hz at all times (Figure S3). LS04 is located to the north of the geyser cone, close to thermal pools and the projected surface location of the bubble trap inferred by Vandemeulebrouck et al. (2014).

The spatial migration of tremor sources likely tracks the evolving thermodynamic conditions in the geyser's subsurface (Rudolph et al., 2018). Tremor locations are stable at depths of ~7–10 m through the type-1 preplays but migrate to shallower depths (~5 m) at the beginning of the main eruption. The ascent of tremor locations over ~200 s at the beginning of the main eruption most likely documents bubble collapse at progressively shallower depths in the water column. The instantaneous increase of the infrared signal (Figure 4a) indicates that ascent of tremor locations follows the main eruption and formation of an eruption column. By both removing mass and lowering pressure, and the vertical transport of heat by rising water, we expect that the depth to boiling relative to the vent will decrease. Both processes would allow migration of steam bubbles to progressively shallower depths before they collapse. However, we observe no changes in the tremor locations during successive type-1 preplays within the resolution of our network (Figures 3d–3f). After the liquid-dominated phase of the main eruption (Figure 5), the low amplitudes of tremor and the slow descent and migration of tremor locations in the north-northeast direction are possibly tracking the top of the water column.

We analyzed locations of tremor during periods in which the geyser is either actively discharging liquid and steam at the surface (preplay and main eruption) and during the relaxation phase when the hydrothermal tremor amplitude is clearly above the background noise. However, in the 2010 experiment, Vandemeulebrouck et al. (2014) observed a steady polarization direction for signals recorded at the single seismometer BB01 at all times when the geyser was not actively discharging fluids. They interpreted the steady polarization as a signature of continuous bubble collapse in a bubble trap to the northeast of the geyser vent. Station LS02 was located close to the original position of BB01 in the 2010 experiment (Figure 1). However, the vertical component of LS02 is strongly contaminated by signals produced by a nearby pool in which the water level oscillates over a period of ~72 s (Figures 1 and S4). Assuming the vertical component to be zero, we observe a steady polarization with a strike of ~330° (Figure S11), similar to that observed by Vandemeulebrouck et al. (2014). Wu et al. (2019) tracked the migration of low frequency hydrothermal tremor signals (1–5 Hz) during the recharge period at OFG. To extract weak tremor signals from noise, they cross correlated waveforms at all stations with a reference station assuming dominance of a persistent seismic source close to the reference station. They detected the tremor source migrating to significantly greater depths (~80 m) following the main eruption and then gradually ascending vertically to an approximate depth of 20 m (Wu et al., 2019). The background tremor observed at OFG and the change in tremor source locations are continuous through the eruption cycle. In contrast, we observe strong tremor signals at LSG only during preplays, main eruption, and relaxation phase and definite tremor source migration only in the latter two periods. Therefore, the mechanisms of tremor source migration at the two geysers are likely to be different.

We calculate a point source moment tensor for a representative discrete seismic event constituting harmonic tremor in the type-1 preplay using a range of simple uniform half-space velocity models and low-frequency

waveforms resulting in ~85% fit to the waveforms. To the best of our knowledge, this is the first study trying to estimate moment tensor or model waveforms of hydrothermal tremor in a geyser environment, equivalent to a repeating M_W ~ −2.5 seismic event recorded at distances <30 m. Slower velocity models with $V_S \lesssim 0.6$ km/s predict significant time lag in waveforms at the most distant station LS01 with respect to the closer stations, something that is not observed in recorded waveforms. For models with $V_S \gtrsim 0.8$ km/s, the best locations and the most probable source volumes are at depths $\lesssim$20 m. A large azimuthal gap in station distribution and unaccounted 3-D elastic structure in the source region lead to large uncertainties in the moment tensor, source type, and M_0 estimates. The characterization of the source mechanism of tremor signals at geysers could be significantly improved using better velocity models incorporating the approximate geometry of the conduit (Hutchinson et al., 1997), using numerical methods capable of modeling seismic wave propagation in combined solid-fluid media (Lecoulant et al., 2019), and dense seismic networks (e.g., Wu et al., 2017).

While the main eruption interval at LSG is stable at approximately ~3 hr, there is considerable variability in the number of preplays (~2–8) prior to the main eruption and their temporal evolution (Figure S2 in this study and Figure 3 in Vandemeulebrouck et al., 2014). We identify several systematic features in the preplay sequences. Understanding the role of preplays in the eruption cycle is important because geysers with complex preplay sequences are rare. Variability and bimodal nature of eruptions similar to that displayed by LSG preplays might indicate presence of additional reservoirs and branching in the geyser plumbing system (Namiki et al., 2016). The longer duration type-2 preplays at LSG are the last preplays in sequences with fewer numbers of preplays. Each of the preplay tremor episodes closely follows moderate intensity discharge of water and steam at boiling temperatures that correspond to the local air pressure (Namiki et al., 2016). However, type-2 preplays develop an eruption column for ~1–2 min as inferred from the peak in IR signals (Figure 2b) and observed visually in at least one eruption cycle. Water discharge measurements show that type-2 preplays discharge significantly more water (~20% of the discharge from the main eruption) than type-1 preplays (Namiki et al., 2016). Assuming a steady heat supply into the geyser reservoir from below, the geyser system is expected to contain more heat during a type-2 preplay compared to earlier preplays. This leads to greater mass of water to be discharged, and more vigorously. The significant loss of accumulated water in the geyser reservoir during a type-2 preplay leads to an ~18-min lag time before the main eruption during which the reservoir is recharged with water and the water is sufficiently heated for the main eruption. Qualitatively similar observations have been made at other geysers. At Strokkur geyser, a greater number of eruptions in quick succession leads to a longer waiting time before the next sequence of eruptions (Eibl et al., 2019). At OFG, longer eruptions used to be followed by longer eruption intervals (Kieffer, 1989; Nicholls & Rinehart, 1967). The temporal pattern of erupted mass in the geyser model of Toramaru and Maeda (2013) exhibits time predictability related to the long-term heating and discharge rates. We conclude that the temporal evolution of type-1 and type-2 preplays at LSG is not random.

For eruption sequences with a type-2 preplay, the onset of main eruption tremor is also delayed with respect to the moderate intensity discharge of water prior to the formation of the eruption column by ~50 s (Figures 6d and 6f). Removal of a large quantity of boiling water by the more vigorous type-2 preplay is expected to accelerate the recharge of the geyser, which is driven by the pressure difference between the geyser's recharge cavity and the deeper units supplying water to the geyser (e.g., Kedar et al., 1998). Assuming a steady heat flux into the reservoir, we suggest that the temperature of water entering the geyser's reservoir is lower than the water left after the type-2 preplay, leading to a net lowering of temperature in the geyser's reservoir. Therefore, at the time of a main eruption following a type-2 preplay, vigorous generation of steam bubbles only occurs after a greater mass of water is removed from the top of the conduit to account for the reduced heat or reduced temperature in the deeper part of the geyser plumbing system.

There are considerable similarities in the first ~150 s of the type-2 preplay tremor and tremor at the beginning of the main eruption: (1) tremor amplitudes in the passband ~6–12 Hz (Figure 2), (2) moderate discharge before the tremor begins, followed by formation of a vigorous eruption column with discharge significantly greater than that for type-1 preplays, (3) the behavior of the spectral peak or the dominant tremor frequency (small increase in frequency from ~5 to ~6 Hz in Figure S8), and (4) temporal evolution of dip angles at the two closest stations LS03 and LS05 (Figures S21 and S22). The main differences are as follows: (1) the discharge gradually decreases and the eruption stops at the end of type-2 preplays, (2) tremor in the

~6–12 Hz passband continues for an extended duration at lower amplitudes toward the end of type-2 pre-plays, and (3) dominant tremor frequency increases toward the end of the type-2 preplay unlike the slow semicontinuous decrease for tremor at beginning of the main eruption. Based on the similarities at the beginning of the two episodes, we suggest that a type-2 preplay begins as a main eruption but does not continue through a full eruption. Geyser eruptions require continuous recharge of fluids and heat input. Moderate discharge and overtopping of water from the vent beginning from the first preplay, ~30–45 min before the main eruption, suggest that the geyser system is more or less completely filled with water at the time of the first preplay. However, the geyser system lacks enough thermal energy or heat for vigorous boiling of the entire reservoir of water to go through a full eruption during type-2 preplay. We suggest that the 3-hour time period of the eruption cycle corresponds to the time taken to sufficiently heat the filled deeper reservoir rather than the time taken to fully recharge the reservoir with water.

Using laboratory experiments, Adelstein et al. (2014) observed that preplays transfer latent heat to the eruption conduit, preparing it for major eruptions. Therefore, another interpretation of our observations is that a smaller number of preplays leads to lower thermal energy, and hence, more water needs to be removed to initiate vigorous cavitation, reflected in the greater time lag between the onsets of the main eruption and tremor. While the eruption cycle itself is stable with a repeating interval of ~3 hr $\pm$ 20 min, the distribution and pattern of preplays is intrinsically tied to some aspects of the main eruption. It is possible that water in the conduit is partially or fully evacuated in type-1 and type-2 preplays, respectively, depending on the thermodynamic state of the system. In contrast, a deeper and larger reservoir boils and evacuates in main eruptions with an interval strictly controlled by long-term recharge and heating rates. Significant pressure and temperature gradients might be present in a long and narrow conduit leading to variability in the preplay sequence (Namiki et al., 2016), whereas the larger reservoir is expected to be more uniform in thermodynamic state due to convection, resulting in a stable recurrence time for the main eruption. There are similarities among type-1, type-2 preplays, and main eruptions at LSG compared to small, medium, and large eruptions, respectively, observed in the Adelstein et al. (2014) experiments. The eruption cycle of El Cobreloa Geyser in El Tatio, Chile, bears some resemblance to that of LSG, in which each major eruption is preceded by a series of minor eruptions, but both types of eruptions occur at regular intervals and minor eruptions gradually become more intense prior to major eruptions (Namiki et al., 2014). Namiki et al. (2014) proposed a model in which water in the geyser reservoir boils releasing steam and liquid into the overlying conduit resulting in minor eruptions, thereby warming the conduit and preparing for major eruptions. Eventually, water in the conduit boils in a steam-dominated eruption that empties the conduit. At LSG, lowered pressures from the discharge of water will also promote boiling.

Similar to other studies (Hurwitz et al., 2014; Rojstaczer et al., 2003), we did not find temporal correlations between the duration of the preplay sequences and atmospheric temperature or pressure, or with strains induced by earth tides (supporting information Text S7 and Figures S28 and S29). However, a longer record is needed for more reliable conclusions, especially to document sensitivity to stress perturbations caused by large amplitude seismic waves from distant earthquakes (e.g., Hurwitz et al., 2014; Husen et al., 2004) or seasonal hydrological changes (Hurwitz et al., 2008) as observed at some other geysers. Pool geysers can be sensitive to variations in atmospheric temperature and/or pressure on account of their exposure to the atmosphere (e.g., Dawson et al., 2012; Hurwitz et al., 2008, 2014), whereas cone geysers are expected to isolate the subsurface reservoir from atmospheric effects. It is likely that the geometry and thermodynamic state of the deeper reservoir exclusively control the eruptions at LSG (e.g., Munoz-Saez, Manga, et al., 2015).

4. Conclusions

The objective of our seismic instrument deployment and signal analysis was to understand the dynamics of subsurface multiphase fluids before, during, and after eruptions and identify the role of preplay events in the eruption cycle at Lone Star Geyser. We document hydrothermal tremor that is laterally offset from the geyser vent by ~5 m and extends to depths of 10 m. Despite the significant variability in the preplay sequences displayed by the hydrothermal tremor, the interval between eruptions at LSG is nearly constant (~3 hrs). Tremor sources are 7–10 m below the surface during preplay events and migrate to shallower depths at the onset of main eruptions, likely documenting warming of the conduit by preplay events. During the relaxation stage that follows the end of the main eruption, tremor sources migrate back to depths of 7–

10 m. Tremor sources before, during, and after eruptions appear confined to a specific structure that we infer is the conduit connecting the vent to a deeper reservoir. The tremor is harmonic at some stages of the eruption cycle and is caused by near-periodic repetition of discrete seismic events. The harmonic tremor shows gliding with systematic changes in the fundamental frequency and the overtones. We identify systematic relations among the two types of preplays, discharge, and the main eruption that likely reflect the state of recharge and evolving thermodynamic conditions in the subsurface. Point-source moment tensor fits to low-frequency waveforms (~2–8 Hz) of an individual tremor event using half-space velocity models indicate average $V_S \gtrsim 0.8$ km/s and source depths ~4–20 m. A wide range of moment tensors with primarily positive isotropic and compensated linear vector dipole moments provide an acceptable degree of waveform fits (>84.1%) to the sparse data. Better constraints can be provided by a better spatial distribution and greater number of seismometers.

Data Availability Statement

The data acquired in this study are archived at the Incorporated Research Institutions in Seismology (IRIS) Data Management Center under the network code 1F (http://www.fdsn.org/networks/detail/1F_2014/).

References

Adelstein, E., Tran, A., Munoz-Saez, C., Shteinberg, A., & Manga, M. (2014). Geyser preplay and eruption in a laboratory model with a bubble trap. *Journal of Volcanology and Geothermal Research*, *285*, 129–135. https://doi.org/10.1016/j.jvolgeores.2014.08.005

Almendros, J., & Chouet, B. (2003). Performance of the radial semblance method for the location of very long period volcanic signals. *Bulletin of Seismological Society of America*, *93*(5), 1890–1903. https://doi.org/10.1785/0120020143

Ardid, A., Vera, E., Kelly, C., Manga, M., Munoz-Saez, C., Maksymowicz, A., & Ortega-Culaciati, F. (2019). Geometry of geyser plumbing inferred from ground deformation. *Journal of Geophysical Research: Solid Earth*, *124*, 1072–1083. https://doi.org/10.1029/2018JB016454

Bean, C., Lokmer, I., & O'Brien, G. (2008). Influence of near-surface volcanic structure on long-period seismic signals and on moment tensor inversions: Simulated examples from Mount Etna. *Journal of Geophysical Research*, *113*, B08308. https://doi.org/10.1029/2007JB005468

Belousov, A., Belousova, M., & Nechayev, A. (2013). Video observations inside conduits of erupting geysers in Kamchatka, Russia, and their geological framework: Implications for the geyser mechanism. *Geology*, *41*(4), 387–390. https://doi.org/10.1130/G33366.1

Caylor, J. R. (2020). Shallow seismic modeling of the hydrothermal plumbing system beneath Old Faithful Geyser in the Upper Geyser Basin of Yellowstone National Park, Master's Thesis, University of Texas at El Paso.

Ceccio, S. L., & Brennan, C. E. (1991). Observations of the dynamics and acoustics of travelling bubble cavitation. *Journal of Fluid Mechanics*, *233*, 633–660. https://doi.org/10.1017/s0022112091000630

Cesca, S., Battaglia, J., Dahm, T., Tessmer, E., Heimann, S., & Okubo, P. (2008). Effects of topography and crustal heterogeneities on the source estimation of LP event at Kilauea volcano. *Geophysical Journal International*, *172*, 1219–1236. https://doi.org/10.1111/j.1365-246X.2007.03695.x

Chouet, B. A. (1996). New methods and future trends in seismological volcano monitoring. In R. Scarpa & R. Tilling (Eds.), *Monitoring and Mitigation of Volcano Hazards* (pp. 23–97). New York: Springer-Verlag.

Chouet, B. A., & Matoza, R. S. (2013). A multi-decadal view of seismic methods for detecting precursors of magma movement and eruption. *Journal of Volcanology and Geothermal Research*, *252*, 108–175. https://doi.org/10.1016/j.jvolgeores.2012.11.013

Cros, E., Roux, P., Vandemeulebrouck, J., & Kedar, S. (2011). Locating hydrothermal acoustic sources at Old Faithful Geyser using matched field processing. *Geophysical Journal International*, *187*, 385–393. https://doi.org/10.1111/j.1365-246X.2011.05147.x

Dawson, P. B., Benítez, M. C., Lowenstern, J. B., & Chouet, B. A. (2012). Identifying bubble collapse in a hydrothermal system using hidden Markov models. *Geophysical Research Letters*, *39*, L01304. https://doi.org/10.1029/2011GL049901

Eibl, E. P., Hainzl, S., Vesely, N. I., Walter, T. R., Jousset, P., Hersir, G. P., & Dahm, T. (2019). Eruption interval monitoring at Strokkur Geyser Iceland. *Geophysical Research Letters*, *47*, e2019GL085266. https://doi.org/10.1029/2019GL085266

Hellweg, M. (2000). Physical models for the source of Lascar's harmonic tremor. *Journal of Volcanology and Geothermal Research*, *101*, 183–198. https://doi.org/10.1016/s0377-0273(00)00163-3

Herrmann, R. B. (2013). Computer programs in seismology: An evolving tool for instruction and research. *Seismological Research Letters*, *84*, 1081–1088. https://doi.org/10.1785/0220110096

Hotovec, A. J., Prejean, S. G., Vidale, J. E., & Gomberg, J. (2013). Strongly gliding harmonic tremor during the 2009 eruption of Redoubt Volcano. *Journal of Volcanology and Geothermal Research*, *259*, 89–99. https://doi.org/10.1016/j.jvolgeores.2012.01.001

Hudson, J. A., Pearce, R. G., & Rogers, R. M. (1989). Source type plot for inversion of the moment tensor. *Journal of Geophysical Research*, *94*(B1), 765–774. https://doi.org/10.1029/jb094ib01p00765

Hurwitz, S., Kumar, A., Taylor, R., & Heasler, H. (2008). Climate-induced variations of geyser periodicity in Yellowstone National Park, USA. *Geology*, *36*, 451–454. https://doi.org/10.1130/G24723A.1

Hurwitz, S., & Manga, M. (2017). The fascinating and complex dynamics of geyser eruptions. *Annual Review of Earth and Planetary Sciences*, *45*, 31–59. https://doi.org/10.1146/annurev-earth-063016-015605

Hurwitz, S., Sohn, R. A., Lutrell, K., & Manga, M. (2014). Triggering and modulation of geyser eruptions in Yellowstone National Park by earthquakes, earth tides and weather. *Journal of Geophysical Research*, *119*, 1718–1737. https://doi.org/10.1002/2013JB010803

Husen, S., Taylor, R., Smith, R. B., & Healser, H. (2004). Changes in geyser eruption behavior and remotely triggered seismicity in Yellowstone National Park produced by the 2002 M 7.9 Denali fault earthquake, Alaska. *Geology*, *32*(6), 537–540. https://doi.org/10.1130/G20381.1

Hutchinson, R. A., Westphal, J. A., & Kieffer, S. W. (1997). In situ observations of Old Faithful Geyser. *Geology*, *25*(10), 875–878. https://doi.org/10.1130/0091-7613(1997)025<0875:isooof>2.3.co;2

Johnson, J. B., & Lees, J. M. (2000). Plugs and chugs—Seismic and acoustic observations of degassing explosions at Karymsky, Russia and Sangay, Ecuador. *Journal of Volcanology and Geothermal Research*, *101*, 67–82. https://doi.org/10.1016/s0377-0273(00)00164-5

Jost, M. L., & Herrmann, R. B. (1989). A student's guide to and review of moment tensors. *Seismological Research Letters*, *60*(2), 37–57. https://doi.org/10.1785/gssrl.60.2.37

Jurkevics, A. (1988). Polarization analysis of three-component array data. *Bulletin of Seismological Society of America*, *78*(5), 1725–1743.

Karlstrom, L., Hurwitz, S., Sohn, R., Vandemeulebrouck, J., Murphy, F., Rudolph, M. L., et al. (2013). Eruptions at Lone Star Geyser, Yellowstone National Park, USA: 1. Energetics and eruption dynamics. *Journal of Geophysical Research*, *118*, 4048–4062. https://doi.org/10.1002/jgrb.50251

Kawakatsu, H. (1998). On the realtime monitoring of the long-period seismic wavefield. *Bulletin of the Earthquake Research Institute, University of Tokyo*, *73*, 267–274.

Kedar, S., Kanamori, H., & Sturtevant, B. (1998). Bubble collapse as the source of tremor at Old Faithful Geyser. *Journal of Geophysical Research*, *103*, 24,283–24,299. https://doi.org/10.1029/98JB01824

Kedar, S., Sturtevant, B., & Kanamori, H. (1996). The origin of harmonic tremor at Old Faithful geyser. *Nature*, *379*, 708–711. https://doi.org/10.1038/379708a0

Kieffer, S. W. (1984). Seismicity of Old Faithful geyser: An isolated source of geothermal noise and possible analogue of volcanic seismicity. *Journal of Volcanology and Geothermal Research*, *22*, 59–95. https://doi.org/10.1016/0377-0273(84)90035-0

Kieffer, S. W. (1989). Geologic nozzles. *Reviews of Geophysics*, *27*(1), 3–38. https://doi.org/10.1029/rg027i001p00003

Kumagai, H., Maeda, Y., Ichihara, M., Kame, N., & Kusakabe, T. (2014). Seismic moment and volume change of a spherical source. *Earth, Planets and Space*, *66*(1), 1–10. https://doi.org/10.1186/1880-5981-66-7

Lecoulant, J., Guennou, C., Guillon, L., & Royer, J.-Y. (2019). Three-dimensional modeling of earthquake generated acoustic waves in the ocean in simplified configurations. *The Journal of the Acoustical Society of America*, *146*(3), 2113–2123. https://doi.org/10.1121/1.5126009

Lesage, P., Mora, M. M., Alvarado, G. E., Pacheco, J., & Métaxian, J.-P. (2006). Complex behavior and source model of the tremor at Arenal volcano, Costa Rica. *Journal of Volcanology and Geothermal Research*, *157*, 49–59. https://doi.org/10.1016/j.jvolgeores.2006.03.047

Lu, N. Q., Prosperetti, A., & Yoon, S. W. (1990). Underwater noise emissions from bubble clouds. *IEEE Journal of Oceanic Engineering*, *15*, 275–281. https://doi.org/10.1109/48.103521

Minson, S. E., & Dreger, D. S. (2008). Stable inversions for complete moment tensor. *Geophysical Journal International*, *174*(2), 585–592. https://doi.org/10.1111/j.1365-246X.2008.03797.x

Munoz-Saez, C., Manga, M., Hurwitz, S., Rudolph, M. L., Namiki, A., & Wang, C.-Y. (2015). Dynamics within geyser conduits, and sensitivity to environmental perturbations: Insights from a periodic geyser in the El Tatio geyser field, Atacama Desert, Chile. *Journal of Volcanology and Geothermal Research*, *292*, 41–55. https://doi.org/10.1016/j.jvolgeores.2015.01.002

Munoz-Saez, C., Namiki, A., & Manga, M. (2015). Geyser eruption intervals and interactions: Examples from El Tatio, Atacama, Chile. *Journal of Geophysical Research: Solid Earth*, *120*, 7490–7507. https://doi.org/10.1002/2015JB012364

Namiki, A., Munoz-Saez, C., & Manga, M. (2014). El Cobreloa: A geyser with two distinct eruption styles. *Journal of Geophysical Research*, *119*, 6229–6248. https://doi.org/10.1002/2014JB011009

Namiki, A., Ueno, Y., Hurwitz, S., Manga, M., Munoz-Saez, C., & Murphy, F. (2016). An experimental study of the role of subsurface plumbing on geothermal discharge. *Geochemistry, Geophysics, Geosystems*, *17*, 3691–3716. https://doi.org/10.1002/2016GC006472

Nayak, A., & Dreger, D. S. (2014). Moment tensor inversion of seismic events associated with the sinkhole at Napoleonville salt dome, Louisiana. *Bulletin of the Seismological Society of America*, *104*(4), 1763–1776. https://doi.org/10.1785/0120130260

Nayak, A., & Dreger, D. S. (2015). Source-type-specific inversion of moment tensors. *Bulletin of Seismological Society of America*, *105*(6), 2987–3000. https://doi.org/10.1785/0120140334

Nayak, A., & Dreger, D. S. (2018). Source inversion of seismic events associated with the sinkhole at Napoleonville salt dome, Louisiana using a 3-D velocity model. *Geophysical Journal International*, *214*, 1808–1829. https://doi.org/10.1093/gji/ggy202

Nicholls, H. R., & Rinehart, J. S. (1967). Geophysical study of geyser action in Yellowstone National Park. *Journal of Geophysical Research*, *72*(18), 4651–4663. https://doi.org/10.1029/jz072i018p04651

Powell, T. W., & Neuberg, J. (2003). Time dependent features in tremor spectra. *Journal of Volcanology and Geothermal Research*, *128*, 177–185. https://doi.org/10.1016/s0377-0273(03)00253-1

Rayleigh, L. (1917). On the pressure developed in a liquid during the collapse a spherical cavity. *Philosophical Magazine*, *34*, 94–98. https://doi.org/10.1080/14786440808635681

Rinehart, J. S. (1965). Earth tremors generated by Old Faithful geyser. *Science*, *150*(3695), 494–496. https://doi.org/10.1126/science.150.3695.494

Rojstaczer, S., Galloway, D. L., Ingebritsen, S. E., & Rubin, D. M. (2003). Variability in geyser eruptive timing and its causes: Yellowstone National Park. *Geophysical Research Letters*, *30*, 1953. https://doi.org/10.1029/2003GL017853

Rudolph, M. L., Manga, M., Hurwitz, S., Johnston, M., Karlstrom, L., & Wang, C.-Y. (2012). Mechanics of Old Faithful Geyser, Calistoga, California. *Geophysical Research Letters*, *39*, L24308. https://doi.org/10.1029/2012GL054012

Rudolph, M. L., Sohn, R. A., & Lev, E. (2018). Fluid oscillations in a laboratory geyser with a bubble trap. *Journal of Volcanology and Geothermal Research*, *368*, 100–110. https://doi.org/10.1016/j.jvolgeores.2018.11.003

Toramaru, A., & Maeda, K. (2013). Mass and style of eruptions in experimental geysers. *Journal of Volcanology and Geothermal Research*, *257*, 227–239. https://doi.org/10.1016/j.jvolgeores.2013.03.018

Trovato, C., Lokmer, I., de Martin, F., & Aochi, H. (2016). Long period (LP) events on Mt Etna volcano (Italy): The influence of velocity structures on moment tensor inversion. *Geophysical Journal International*, *207*, 785–810. https://doi.org/10.1093/gji/ggw285

Tsuruoka, H., Kawakatsu, H., & Urabe, T. (2009). GRiD MT (grid-based real-time determination of moment tensors) monitoring the long period seismic wavefield. *Physics of the Earth and Planetary Interiors*, *175*, 8–16. https://doi.org/10.1016/j.pepi.2008.02.014

Vandemeulebrouck, J., Roux, P., & Cros, E. (2013). The plumbing of Old Faithful Geyser revealed by hydrothermal tremor. *Geophysical Research Letters*, *40*, 1989–1993. https://doi.org/10.1002/grl.50422

Vandemeulebrouck, J., Sohn, R. A., Rudolph, M. L., Hurwitz, S., Johnston, M. J. S., Soule, S. A., et al. (2014). Eruptions at Lone Star Geyser, Yellowstone National Park, USA, Part 2: Geophysical constraints on subsurface dynamics. *Journal of Geophysical Research*, *119*, 8688–8707. https://doi.org/10.1002/2014JB011526

Vavrycuk, V. (2013). Is the seismic moment tensor ambiguous at a material interface? *Geophysical Journal International*, *194*, 395–400. https://doi.org/10.1093/gji/ggt084

Vidale, J. E. (1986). Complex polarization analysis of particle motion. *Bulletin of Seismological Society of America*, *76*(5), 1393–1405.

Wang, C. Y., & Herrmann, R. B. (1980). A numerical study of P-, SV- and SH-wave generation in a plane layered medium. *Bulletin of Seismological Society of America*, *70*(4), 1015–1036.

Wu, S. M., Lin, F. C., Farrell, J., & Allam, A. (2019). Imaging the deep subsurface plumbing of Old Faithful geyser from low-frequency hydrothermal tremor migration. *Geophysical Research Letters*, *46*, 7315–7322. https://doi.org/10.1029/2018GL081771

Wu, S.-M., Ward, K. M., Farrell, J., Lin, F.-C., Karplus, M., & Smith, R. B. (2017). Anatomy of Old Faithful from subsurface seismic imaging of the Yellowstone Upper Geyser Basin. *Geophysical Research Letters*, *44*, 10,240–10,247. https://doi.org/10.1002/2017GL075255

Yoon, S. W., Crum, L. A., Prosperetti, A., & Lu, N. Q. (1991). An investigation of the collective oscillations of a bubble cloud. *Journal of Acoustical Society of America*, *89*, 700–706. https://doi.org/10.1121/1.1894629

Zhu, L., & Ben-Zion, Y. (2013). Parametrization of general seismic potency and moment tensors for source inversion of seismic waveform data. *Geophysical Journal International*, *194*, 839–843. https://doi.org/10.1093/gji/ggt137

References From the Supporting Information

Agnew, D. C. (1997). NLOADF: A program for computing ocean-tide loading. *Journal of Geophysical Research*, *102*, 5109–5110. https://doi.org/10.1029/96JB03458

Agnew, D. C. (2012). *SPOTL: Some Programs for Ocean-Tide Loading*. San Diego: SIO Technical Report, Scripps Institution of Oceanography. Retrieved from https://igppweb.ucsd.edu/~agnew/Spotl/spotlman.pdf

Brocher, T. M. (2008). Key elements of regional seismic velocity models for long period ground motion simulations. *Journal of Seismology*, *12*(2), 217–221. https://doi.org/10.1007/s10950-007-9061-3

Havskov, J., & Ottemöller, L. (2010). Location. In *Routine Data Processing in Earthquake Seismology* (pp. 103–104). Springer.

Ingebritsen, S. E., & Rojstaczer, S. A. (1996). Geyser periodicity and the response of geysers to deformation. *Journal of Geophysical Research*, *101*, 21,891–21,905. https://doi.org/10.1029/96JB02285

Munoz-Saez, C., Saltiel, S., Manga, M., Nguyen, C., & Gonnermann, H. (2016). Physical and hydraulic properties of modern sinter deposits: El Tatio, Atacama. *Journal of Volcanology and Geothermal Research*, *325*, 156–168. https://doi.org/10.1016/j.jvolgeores.2016.06.026

Schimmel, M., & Gallart, J. (2007). Frequency-dependent phase coherence for noise suppression in seismic array data. *Journal of Geophysical Research*, *112*, B04303. https://doi.org/10.1029/2006JB004680

Schimmel, M., Stutzmann, E., & Gallart, J. (2011). Using instantaneous phase coherence for signal extraction from ambient noise data at a local to a global scale. *Geophysical Journal International*, *184*, 494–506. https://doi.org/10.1111/j.1365-246X.2010.04861.x